Simulation based evaluation of time-variant loadings acting on tunnel linings during mechanized tunnel construction

Jelena Ninić[a], Günther Meschke[b,*]

[a] *Centre for Structural Engineering and Informatics, The University of Nottingham, UK*
[b] *Institute for Structural Mechanics, Ruhr University Bochum*

Abstract

In the design of machine driven tunnels, the loadings acting on the segmental lining are often adopted according to simplified assumptions, which improperly reflect the actual loading on the linings developing during the construction of a bored tunnel. A coupled 3D Finite Element model of the tunnel advancement process including the ring-wise installation of the lining and the hardening process of the grouting material serves as the basis for the analysis of the actual spatio-temporal evolution of the loading on the lining during tunnel construction. The distribution of the loadings in the different construction phases is calculated using a modified surface-to-surface contact condition imposed between the solidifying grouting material in the tail gap and the lining elements. An extensive parametric study investigates the influence of the initial grouting pressure, the pressure gradient, the temporal stiffness evolution, the soil permeability as well as the interface conditions between the grouting material and the tunnel shell on the temporal evolution of the loading on linings.

Keywords: Mechanized tunneling, Tunnel lining, Loading, Grouting pressure, Solidification, Process-oriented FE simulation, Soil permeability

*Corresponding author. Tel.: +49 234 3229051; fax: +49 234 3214149
Email address: guenther.meschke@rub.de (Günther Meschke)
URL: www.sd.rub.de (Günther Meschke)

1. Introduction

In mechanized tunneling, the tunnel shell is installed ring-wise during the still stand of the Tunnel Boring Machine (TBM) by assembling individual lining segments through an erector (19). The tunnel shell is in contact with the surrounding soil via the grouting mortar, injected into the tail gap between the outside face of the lining and the soil immediately after ring installation. As the front face of the new lining ring is used as the support for pushing the TBM forward by hydraulic jacks after each ring installation, tunnel linings in machine driven tunnel construction are subjected to construction loadings (the jack forces) in addition to the time variant loadings acting along the outside surface due to the pressurized grouting mortar, whose stiffness increases and eventually transfers the stresses from the ground and the groundwater to the lining.

In engineering practice, the design of tunnel linings is in general based upon analytical solutions or simplified numerical models. Analytical solutions typically are based upon the following assumptions: (a) 2D plane strain assumption, (b) the soil stresses are equal to in-situ stress in the undistributed ground, (c) the soil and lining are elastic materials, (d) the lining has a perfect circular geometry, (e) the soil-structure interaction is neglected and (f) the internal forces in radial and tangential directions are independent from the forces in axial direction (23; 9; 6). In more advanced semi- analytical structural analysis models some of the oversimplifications addressed above are accounted for by considering non-linear ground behavior (14), soil-structure interaction effects by means of numerically determined ground reaction curves (10), staged beam construction and longitudinal bending moments (31) as well as non-linear longitudinal and ring joints (5). However, evidently, analytical and semi-analytical models have limitations in regards to a realistic incorporation of all relevant interactions between the tunnel shell and the surrounding soil.

Often Finite Element (FE) models are used for the analysis of tunnel linings, representing the lining by structural elements (beam, shell or solid elements), bedded on elastic springs to represent the soil resistance, considering design loads provided by guidelines (2; 13; 28; 15; 8). The International Tunneling Association (ITA) published *Guidelines for the Design of Shield Tunnel Lining* in 2000 (12), suggesting to consider the following design loads: geostatical loads, thrust jacking loads, trailer and other service loads, secondary grouting loads, dead load, storage and erection loads. The geostatical loads include the effective in situ stresses in undisturbed state, the water pressure, the dead load of the lining, surcharge load (road and railway traffic load and buildings weight) and subgrade reaction, which

depends on the ground stiffness and rigidity of lining. Although the guidelines suggest the consideration of construction loads such as thrust forces of hydraulic jacks, back-fill grouting, erector operation and segment transport loads, the temporal changes of the loading conditions during different construction phases are not considered in existing empirical load models. Due to the changing stiffness of the grouting mortar with time, the stress distribution around the tunnel lining and, consequently, the loadings acting on the lining structure are affected. Also, the dissipation of water pressures, which constitutes a strongly time-dependent process primarily controlled by the soil permeability, affects the loading conditions. Investigation of the changing loading conditions during the construction phase by means of numerical simulations is the main subject of the present paper.

Despite the fact that constant monitoring is usually performed during the tunnel advance, only in few cases the loads affecting the segments are measured for closed-type shield tunnels. In (17) is given an overview of ten projects, during which the earth and the water pressure acting on the tunnel lining in the circumferential direction have been measured for tunnels in sandy soils, clayey soils, gravel in both alluvium and diluvium. The general conclusion drawn form the analysis of measured data, is that the earth pressure developed during the construction, as well as the steady state condition depend on (a) the ground conditions, (b) the ground water table, (c) tunneling-induced deformations of the ground, (d) the magnitude of the back-fill grouting pressure, (e) the operational control, (f) construction phase and (g) the tunnel alignment.

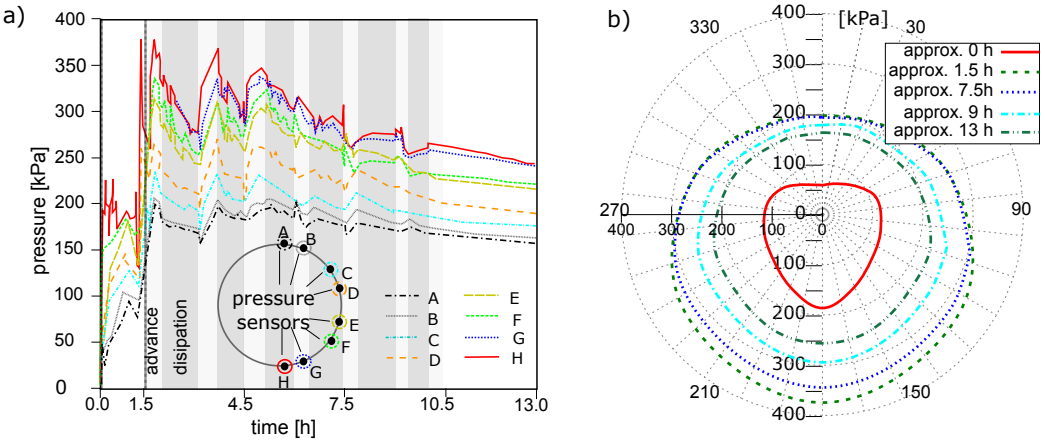

Figure 1: Results from measurements of the evolution of the grouting pressure in time: a) grouting pressures for pressure sensors A–H from the Sophia Rail tunnel; b) pressures at different construction stages (Figure adapted by authors from (3)).

As regards to short term loading on tunnel linings due to the pressurization of the tail gap, results from monitoring are evaluated in (11; 17; 3). As shown in Figure 1, containing measurements from the Sophia Rail tunnel in the Netherlands (3), the loading on the lining is constantly changing during construction. It was observed, that the grouting pressure increases during the drilling time and decreases during the standstill due to "bleeding" of the grouting (i.e. infiltration), as highlighted in Figure 1. Furthermore, fluctuations of the grouting pressure occur due to the changing volume of the tail gap, as was observed in particular during the advancement of a curved tunnel alignment (4).

As the actual loadings acting on the tunnel linings in mechanized tunneling experience significant changes in time, there is evidently a need for a more detailed investigation of the actual distribution of the loadings acting on tunnel linings during the construction process and their temporal evolution resulting from the interactions of the lining with the tail void grouting, the surrounding soil, and the TBM advancement. Therefore, in this paper the evolution of the loadings acting on tunnel linings is evaluated by means of a process-oriented simulation model for mechanized tunneling (25; 26). This simulation model realistically considers all construction stages as well as all relevant components and time-dependent processes (groundwater flow, hydration of cement-based grouting mortars) involved in the tunneling process and is therefore well suited for the evaluation of the loadings on the linings. The earth and water pressure is obtained through a contact interface imposed between the lining and the grouting mortar in each step of the tunnel construction process. The pressure changes continuously from the moment of the ring installation to its steady state.

The remainder of the paper is organized as follows: Section 2 contains a brief summary of the numerical simulation model used for the evaluation of the loading on the lining and the lining forces. The effect of the soil and grout properties and of selected process parameters on the induced loadings on the tunnel lining and their temporal evolution are discussed in Section 3. In Section 4 the influence of the properties of the interface between the lining and the grouting mortar is investigated. The findings from this computational study and their consequences for the lining design are summarized in the Conclusions.

2. Computational model for soil-structure interaction in mechanized tunneling

2.1. Simulation model for mechanized tunneling

For the numerical simulation of machine driven tunnel advance the process-oriented 3D simulation model `ekate` proposed in (25; 22) is employed. It is based upon the object-oriented FE framework KRATOS (7) and takes into consideration all important components of the shield tunneling processes and their mutual interactions (1). The components of this simulation model are shown in Figure 2.

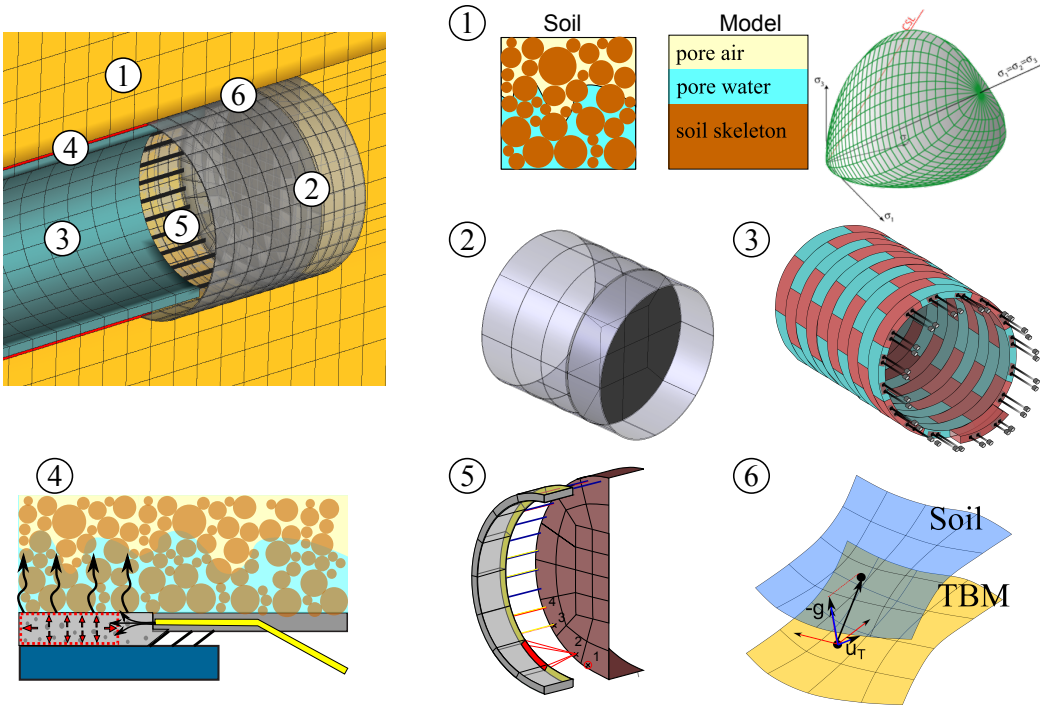

Figure 2: Finite element model for shield tunneling `ekate` and its components: (1) surrounding soil, (2) TBM, (3) segmented lining, (4) pressurized grouting material with time-dependent properties, (5) hydraulic jacks used for the advancement of the TBM, and (6) frictional contact between the shield skin and the soil.

The Tunnel Boring Machine (TBM) is represented as a deformable body moving through the soil and interacting with the ground through frictional surface-to-surface contact, allowing that the deformation of the soil naturally follows the real, tapered geometry of the TBM and captures the effect of overcutting. The tunnel

advance is modeled by means of deactivation of soil elements and installation of tunnel lining and grouting elements while at the same time the TBM is advanced by hydraulic jacks thrust. The soil is modeled as a two (three)-phase fully (partially) saturated material (25), accounting for the solid, the pore water and pore air as distinct phases according to the theory of mixtures. In the analyses contained in this paper, fully saturated conditions are assumed. Hence, the total stresses are obtained according to

$$\sigma = \sigma' - \mathbf{I} p_w, \tag{1}$$

with σ' as the effective stresses of the soil skeleton and p_w as the pore water pressure (25). For the modeling of the inelastic soil behavior, two types of elasto-plastic constitutive models are available (the Drucker-Prager and the Clay and Sand Model (33)). To provide the stability of the tunnel face and to reduce ground loss behind the tapered shield, a face support pressure and the grouting pressure are applied at the tunnel face and in the steering gap, respectively.

2.1.1. Two-field finite element formulation

For both fully saturated soft soils as well as for the modeling of the grouting mortar a two-field finite element formulation is implemented. The governing equations of this model are given by the weak formulation of the mass balance equation δW_w for the water flow in the pore space of the soil and the grout, respectively, and the weak form of the equilibrium equation δW_m:

$$\delta W_w = \delta W_{w,int} - \delta W_{w,ext} = 0\,, \qquad \delta W_m = \delta W_{m,int} - \delta W_{m,ext} = 0\,, \tag{2}$$

with

$$\begin{aligned} \delta W_{w,int} &= \int_\Omega \delta p_w \mathbf{I} : \dot{\varepsilon}\, \mathrm{d}\Omega\,, \qquad \delta W_{w,ext} = \int_\Omega \delta \nabla p_w \cdot \mathbf{q}\, \mathrm{d}\Omega - \int_{\Gamma_q} \delta p_w q^*\, \mathrm{d}\Gamma_q \\ \delta W_{m,int} &= \int_\Omega \delta\varepsilon : \left(\sigma' + \mathbf{I} p_w\right) \mathrm{d}\Omega\,, \quad \delta W_{m,ext} = \int_\Omega \delta \mathbf{u} \cdot \rho \mathbf{g}\, \mathrm{d}\Omega - \int_{\Gamma_\sigma} \delta \mathbf{u} \cdot \mathbf{t}^*\, \mathrm{d}\Gamma_\sigma \end{aligned} \tag{3}$$

ε denotes the strain tensor, $\mathbf{q}$ the pore water flow and q^* the prescribed flow through the boundary. σ is the total stress tensor, ρ the density of the mixture, $\mathbf{g}$ the gravitational acceleration and $\mathbf{t}^*$ the traction vector. p_w and $\mathbf{u}$ denote the pore water pressure and the displacements of the soil and the grouting, respectively.

2.2. *Tail void grouting*

The annular gap between the segmented lining tube and the excavation boundary, illustrated in Figure 3, is filled with a pressurized grouting mortar modeled as a fully saturated two-phase material with a hydrating matrix phase, considering the temporal evolution of the elastic stiffness and the permeability of the cementitious grout (21). This two-phase element is based upon the weak form of the balance of momentum and the balance of fluid mass occupying the pore volume in conjunction with a time variant constitutive model for the solidifying grouting material, linearized geometrical relations and the Darcy law governing the fluid flow in the grouting material. As the transition of cementitious grouting mortar from a liquid to solid state plays a crucial role in maintaining the stress state of the surrounding soil and controlling the settlements, a constitutive model is applied that accounts for the time-dependent material behavior of grouting mortar in the simulation model.

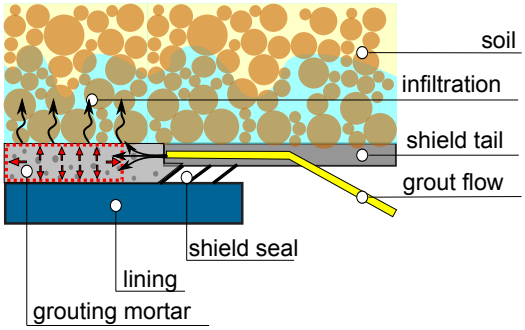

Figure 3: Tail gap grouting: sketch of the grouting of the annular gap between the lining and the surrounding soil with a pressurized mortar injected through the shield skin.

2.2.1. *Solidification model for the grouting material*

Within the simulation model, the pressurization of the grouting mortar is accounted for by using a two-phase formulation accounting for the effective stresses σ' in the gradually stiffening solid phase and for the liquid pressure p of the fluid phase. The changing material properties resulting from hydration of cementitious grouting mortars are represented by time-dependent material properties for the stiffness and the permeability. The formulation is based on a model for shotcrete proposed by (21), where the total strain ε is split into the elastic strain ε^e and an irreversible strain due to time-dependent solidification ε^t:

$$\varepsilon = \varepsilon^e + \varepsilon^t \tag{4}$$

The stiffening effect observed in grouting materials is incorporated in a 3D hyperelastic law by means of a time-dependent function of the stored energy

$$W(\boldsymbol{\varepsilon}^e,t) = \frac{1}{2}\left(\boldsymbol{\varepsilon}-\boldsymbol{\varepsilon}^t\right) : \mathbb{C}^{28} : \left(\boldsymbol{\varepsilon}-\boldsymbol{\varepsilon}^t\right). \tag{5}$$

where $\mathbb{C}^{28}$ is the elastic stiffness tensor after 28 days and $\boldsymbol{\varepsilon}^t$ are irreversible aging induced strains (21). Introducing a time-dependent material tensor

$$\mathbb{C} = \mathbb{C}^{(28)}\frac{E(t)}{E(28)}, \tag{6}$$

the effective stresses at a certain time instant t_{n+1} is derived from the stored energy function Eq.(5) as

$$\boldsymbol{\sigma}'_{n+1} = \mathbb{C}^{(28)} : \left(\boldsymbol{\varepsilon}_{n+1}-\boldsymbol{\varepsilon}^t_{n+1}\right), \tag{7}$$

with the irreversible aging-induced strains determined as

$$\boldsymbol{\varepsilon}^t_{n+1} = \boldsymbol{\varepsilon}^t_n + (1-\frac{\xi}{E^{(28)}\Delta t})\Delta\boldsymbol{\varepsilon}, \tag{8}$$

with $\xi = \int_{t_n}^{t_{n+1}} E(t)\,dt$ determined from integration of the time dependent elastic modulus within the time interval $[t_n, t_{n+1}]$. The time dependent stress-strain behavior of the grouting mortar is based upon the time variant formulation for the elastic modulus, which according to (21), is defined as $E(t) = \beta_E(t)E^{(28)}$. The coefficient $\beta_E(t)$ is given as:

$$\beta_E(t) = \begin{cases} \beta_E^I = & c_E t + d_E t^2 & \text{for} \quad t \le t_E\,, \\ \beta_E^{II} = & (a_E - \frac{b_E}{t_E - \Delta t_E})^{-0.5} & \text{for} \quad t_E < t \le 672\,h\,, \\ \beta_E^{III} = & 1.0 & \text{for} \quad t > 672\,h\,. \end{cases}$$

In the expression for $\beta_E(t)$, the parameters a_E, b_E, d_E, and c_E depend on the ratio $E^{(1)}/E^{(28)}$, the initial time interval t_E for hydration of grouting mortar and the time step Δt_E (see (21) for details).

During hydration of cementitious grouting mortars, the permeability of the porous material changes. In the model, an exponential relation between the initial permeability of the grouting mortar $k^{(0)}$ and the permeability after 28 days $k^{(28)}$ is used:

$$k(t) = (k^{(0)} - k^{(28)})e^{-\beta_{grout}\,t} + k^{(28)}, \tag{9}$$

with the transition coefficient β_{grout} adjusted to experimental results. For the numerical studies in this paper the following values of the parameters describing

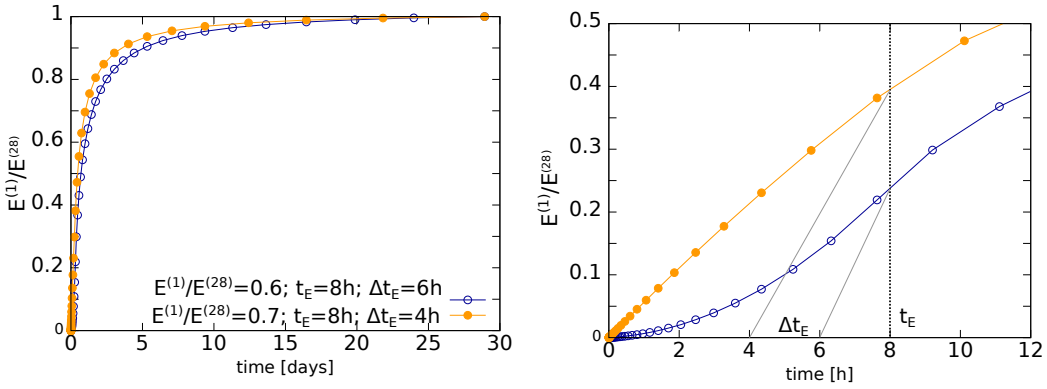

Figure 4: Evolution of the elastic stiffness of the grouting mortar in time.

time-variant permeability of the grouting mortar are adopted: $k^{(0)} = 10^{-4}\,m/s$, $k^{(28)} = 10^{-8}\,m/s$ and $\beta_{grout} = 0.0535$. This formulation allows to account for the pressurization of the grout during stepwise installation of the lining rings and prescription of equivalent pressure boundary conditions at the front side of the finite elements representing the grouting material in the tail gap.

2.2.2. Numerical tests of the constitutive model for the grouting mortar

The constitutive model for the grouting mortar is investigated for different loading paths and hydration properties of the material. To this end, uniaxial loading is applied in z-direction on the top face of a two-phase quadrilateral finite element (Figure 5(left)) with the displacements fixed in lateral direction. In this study, the stiffness of the grouting material after 28 days and the ratio of the stiffness after 1 and 28 days are assumed as $E_{28} = 5.25\,MPa$ and $E_1/E_{28} = 0.6$, respectively.

In a first analysis, the element is applied to four different scenarios for the temporal evolution of the axial loading $F_z(t)$ prescribed in the parametrized format:

$$F_z(t) = \frac{1 - e^{-\alpha \cdot \frac{2\pi}{28} \cdot t}}{1 - e^{-\alpha \cdot 2\pi}} \tag{10}$$

Figure 5a shows the four different temporal loading paths applied to the grouting element with a final axial load of 10 kPa prescribed in z-direction. The resulting temporal evolution of the axial deformations in Figure 5b shows, that the loading history has significant influence on the nonlinear evolution of the deformations.

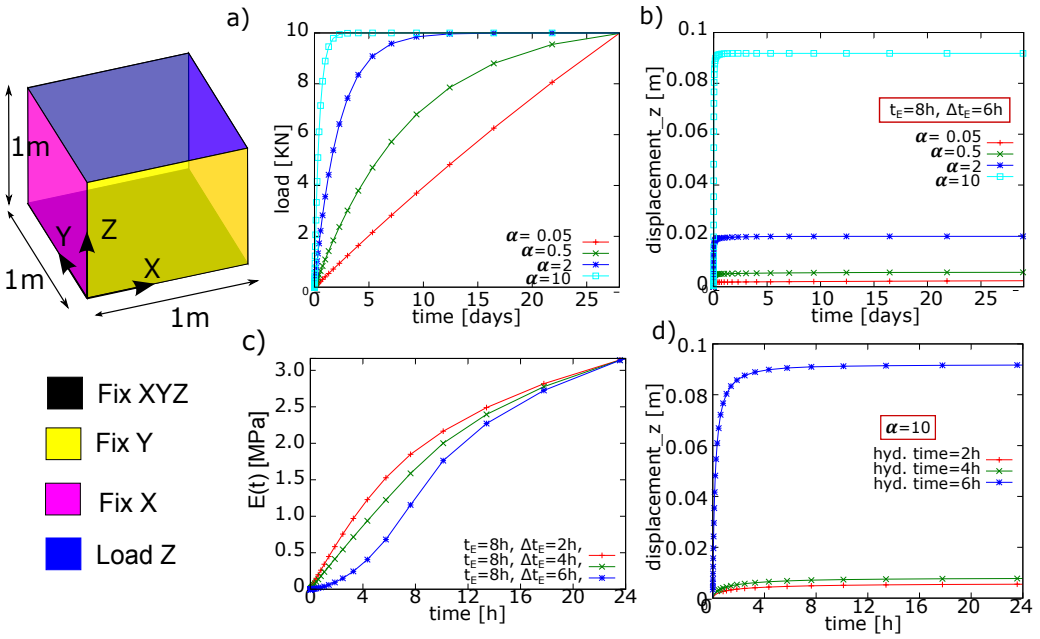

Figure 5: Constitutive model for grouting mortar: a) Four scenarios for the temporal evolution of the axial loading applied to the grouting element ; b) resulting axial deformation of the grouting element for different loading scenarios ; c) Three scenarios for the temporal evolution of the stiffness of the grouting mortar; d) resulting axial deformation of the grouting element for different hydration scenarios (loading case α=10).

In a second parametric study, the effect of the evolution of the grouting stiffness is investigated. Figure 5c shows the temporal evolution of the Young's modulus $E(t)$ for three different parameters Δt_E used in the expression for $E(t)$ ($\Delta t_E = 6\,h$, representing a slow stiffening characteristics, $\Delta t_E = 4\,h$, representing a moderate and $\Delta t_E = 2\,h$, representing a rapid stiffening of the grouting mortar).

In all cases, the hydration time t_E is 8 h. The grout element is subjected to the time-dependent load given in Eqn. 10 with the final load level of 10 kPa and $\alpha = 10$. Figure 5d contains the resulting temporal axial deformation for the three stiffening characteristics. A strong influence of the stiffness evolution on the temporal development and the asymptotic level of the axial deformations is observed. The asymptotic deformations for the slowest stiffening ($\Delta t_E = 6\,h$) is approximately 16 times larger as compared to the rapid stiffening ($\Delta t_E = 2\,h$).

2.3. *Loadings acting on the tunnel lining*

As the simulation model `ekate` includes all relevant components involved in mechanized tunneling and their mutual interactions, this model can be used as a solid foundation to extract the loadings acting on the lining. The acting loadings on lining can be broadly divided into longitudinal loadings induced by the hydraulic jacks and loadings along the circumference of the tunnel structure induced by the pressure from the grouting mortar and the surrounding soil, respectively (see Figure 6).

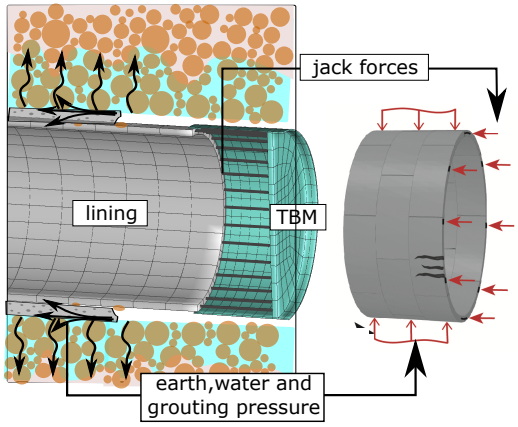

Figure 6: Construction induced loading and the grouting pressure, earth pressure and the groundwater pressure acting on linings in mechanized tunneling.

The construction induced loads due to the high concentrated jack forces acting directly on the front face of the concrete segments may cause local damage (cracking and spalling) (5) with a detrimental effect on the durability. The loadings acting along the outer circumference of the tunnel lining, caused by the pressurized grouting mortar and the soil stresses and the groundwater pressure, determine the global structural behavior of the system. For the proper evaluation of the normal and tangential tractions acting on the outer surface of the lining in the various construction stages a surface-to-surface contact model is used in the computational simulation model `ekate`.

2.3.1. *Surface-to-surface contact formulation*

Contact between the two-phase finite elements representing the grouting mortar and the lining rings is accomplished by means of a surface-to-surface contact formulation introduced by (18). The contact formulation imposes a geometric

constraint between the contacting (”slave”) body (the lining elements) and the contacted (”master”) body (the grouting elements) which controls the interaction between the two bodies with independent deformations. This allows to consider different interface conditions between the grout and the tunnel shell. In this paper, frictionless and fully bonded conditions are investigated.

The surface-to-surface contact algorithm is based on the fulfillment of the contact constraint at each quadrature point on the so-called slave contact surface. The physical requirement of impenetrability is stated in a discrete manner in terms of the gap g (see Figure 7) between the quadrature points of the slave surface $\mathbf{x}^1$ and their closest point projection on the master surface $\mathbf{x}^2$:

$$g(\mathbf{x}^1) = -\nu(\mathbf{x}^1 - \mathbf{x}^2(\mathbf{x}^1)) \tag{11}$$

Herein the gap $g(\mathbf{x}^1)$ is denoted to be positive if penetration occurs and the out-

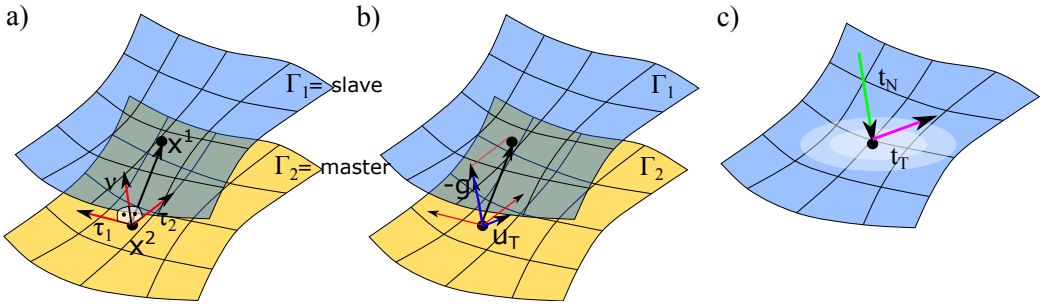

Figure 7: Geometrical representation of surface-to-surface contact: a) Contact partners in deformed configuration; b) Definition of relative normal displacement (gap g) and relative tangential displacement u_t; c) Contact forces.

ward normal ν is computed explicitly and held fixed during the solution within a time step. The second constraint assumes compressive interactions between the contacting bodies. Both impenetrability and compressibility constraint are stated in terms of Kuhn-Tucker optimality conditions.

In the context of a nonlinear finite element analysis of the tunnel advance, the augmented LAGRANGE method (18) is used to solve the constrained problem consisting of a two-fold scheme: first, while solving the global equilibrium equation iteratively, fulfillment of the contact constraint is enforced by penalizing a violation with a high penalty potential. Secondly, after solution of the global equilibrium, the LAGRANGE multiplier used to express the contact force is updated. This scheme can be repeated until the violation of the contact constraint

satisfies a pre-defined criterion. By use of the augmented LAGRANGE method, the contact potential is expressed in terms of the contact forces λ_N and the contact gap g as:

$$\Pi^{contact} = \sum_{i}^{1,2} \int_{\Gamma_c^i} \left[\frac{1}{2e_N} \langle \lambda_N + e_N g \rangle^2 + \frac{1}{2e_N} {\lambda_N}^2 \right] . \tag{12}$$

e_N is the penalty parameter (see, e.g. (32)). Taking the variation of Eq. 12, an expression for the virtual work associated with the contact forces is obtained. The contact normal force t_N acting between the quadrature points on the lining element facets and their closest point projection on the grouting element facets is computed according to (30) as:

$$t_N = \langle \lambda_N + e_N g \rangle \tag{13}$$

In the finite element formulation, the weak form of the mechanical problem according to Eq.2 is complemented by the virtual work of the contact forces:

$$\delta W_m = \delta W_{m,int} - \delta W_{m,ext} + \delta W_c = 0 , \tag{14}$$

with

$$\delta W_c = \int_{\Gamma_c^{(b)}} [t_N \delta g + t_{T_i} \delta, \mathbf{u}_T] d\Gamma \tag{15}$$

as the contribution of the contact forces to the virtual work. δg and $\delta \mathbf{u}_T$ are the normal and tangential virtual displacements at the contact interface. Details on the implementation of the surface-to-surface contact used in the simulation model `ekate` can be found in (24).

2.3.2. Earth and water pressure acting on linings

To obtain the normal contact pressure acting on the tunnel lining, the contact interface is imposed on the interacting surfaces of the lining and grouting as shown in Figure 8a. The inner surface of the grouting is defined as the master surface, while the outer surface of the lining is defined as the slave contact surface. Here, the focus is on the contact pressure in direction normal to the surface. Forces acting in tangential direction along the outside face of the lining are considered in Section 4. The acting earth and water pressures are obtained as follows:

$$\begin{cases} t_N = \langle \lambda_N + e_N g \rangle & \text{for total earth pressure,} \\ p_{fluid} & \text{for water pressure.} \end{cases} \tag{16}$$

t_N denotes the normal traction; the nodal fluid pressure p_{fluid} is transferred to the quadrature points on the slave surface.

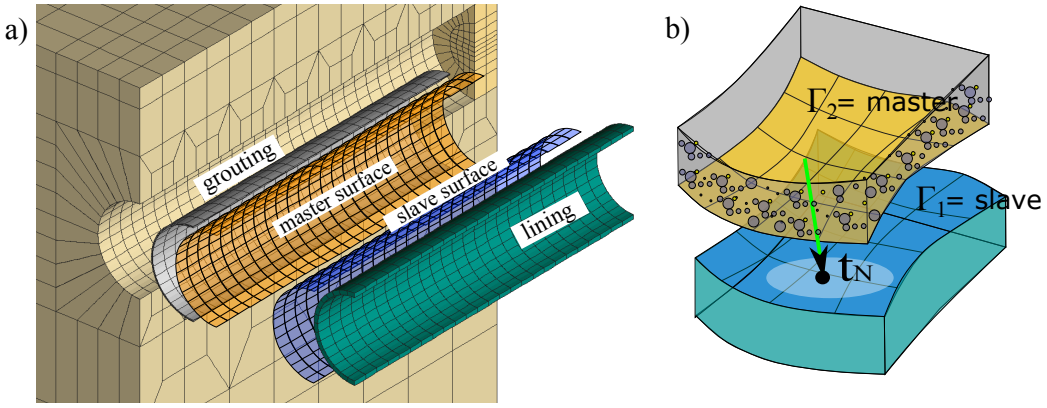

Figure 8: Contact condition between lining and grouting surface: a) discretization of the FE model; b) illustration of the grouting and lining mesh interacting through surface-to-surface contact and resulting contact stress.

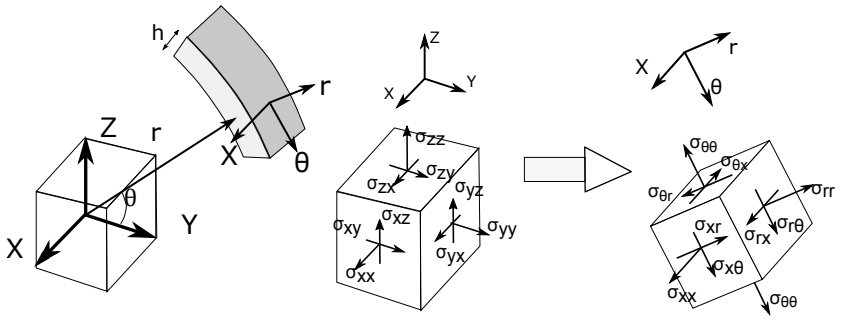

Figure 9: Conversion of stresses from Cartesian to Cylindrical coordinate system.

To evaluate the structural response of the lining shell resulting from the time-variant loadings induced by the construction process and the grouting, earth and water pressures, the normal forces (N) and bending moments (M), are computed by integration of the stresses in the finite elements representing the lining structure. The stresses in lining structure, calculated in the cartesian (X,Y,Z) coordinate system are transformed to cylindrical coordinates (x,r,θ) as shown in Figure

9. The integration of the transformed stresses leads to structural forces:

$$N = \int_{-\frac{h}{2}}^{\frac{h}{2}} \sigma_{\theta\theta} dz \qquad \text{and} \qquad M = \int_{-\frac{h}{2}}^{\frac{h}{2}} \sigma_{\theta\theta} z dz \tag{17}$$

where $\sigma_{\theta\theta}$ are stresses acting in tangential direction. Automated conversion of stresses from cartesian to cylindrical coordinate system and calculation of structural forces for a chosen set of rings is enabled by implementing a *Lining Force Utility* in the framework of `ekate`. A verification analysis of the load transfer model from the soil through the grouting element to the lining based upon a simplified benchmark problem is contained in the Appendix 6.1.

2.4. Loadings acting on linings in steady state: Comparison with in situ stress state

Before proceeding to the 3D tunnel advancement analyses, a 2D plane strain model is created to evaluate the earth pressure acting on the tunnel lining in the steady state. The same tunnel diameter (d= 9.475 m) and overburden (11.5 m) as well as thickness of the linings (t= 0,45 m) as used later in the advancement simulations in Section 3 are adopted. However, here the grouting material is not yet considered, i.e. the surrounding soil is transferring the in situ stresses directly onto the lining shell as illustrated in Figure 10 (Case 2). The static earth pressure acting on the tunnel lining is compared with the in situ earth pressure acting along the excavation boundary as shown in Figure 10 (Case 1). Using the previously described contact algorithm, the normal contact pressure acting on the circumferential excavation boundary is evaluated. The material properties of the soil layers used for this study are summarized in Table 1.

Figure 10 shows the distribution of the total normal contact pressure acting along the installed lining ring (Case 2) and along the excavation boundary in the in situ state (Case 1). The figure demonstrates the considerable influence of the soil-structure interaction on the shape of the total normal pressure acting on the tunnel lining. The magnitude of the normal contact stresses acting on the invert of the lining is considerably smaller as compared to the in situ stress conditions due to the excavated volume of the soil.

For comparison, an analysis is performed, with the soil subgrade reaction represented by elastic springs and the calculated in situ stress applied as external distributed loading, neglecting the soil-structure interaction and the weight of the

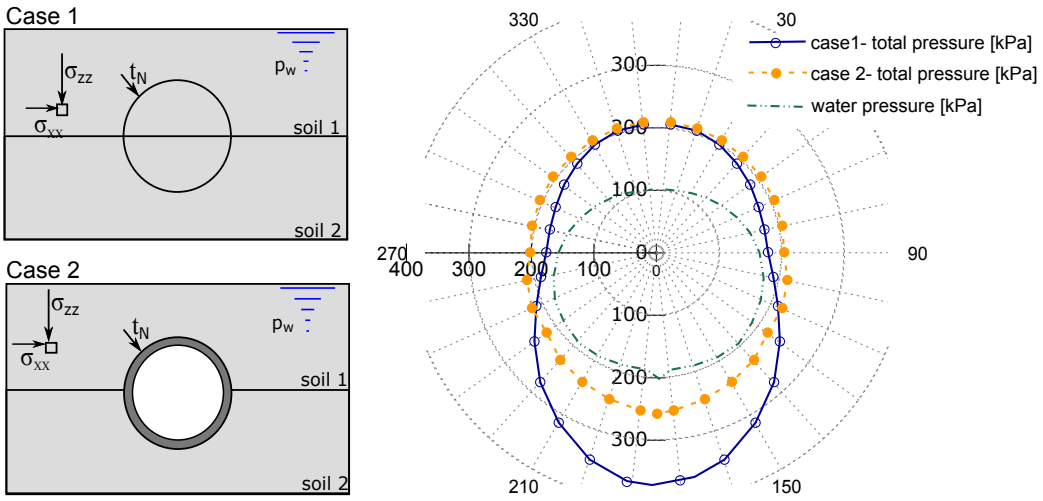

Figure 10: Influence of the presence of the tunnel structure on the loading along the lining boundary: Distribution of the total normal contact pressure acting along the installed lining ring and along the excavation boundary in the in situ state.

excavated soil (Figure 11a). According to (16), the stiffness of the spring is assumed to depend on the stiffness of the soil E, the Poison's ratio ν and the radius of the tunnel lining r:

$$K_s = \frac{E}{r} \frac{1-\nu}{(1+\nu)(1-2\nu)} \tag{18}$$

The finite element discretization of the lining ring and the material parameters for the spring model (Figure 11a) are identical to the soil-structure model (Figure 11b). The soil properties given in Table 1 are used to determine the stiffness of the elastic springs K_s. The loading applied to the lining for the elastic bedding model corresponds to the in situ stresses in the soil (Fig 10, blue line).

Figure 12 contains a comparison of the structural forces (normal force (N) and bending moments (M)) in the lining for the elastic bedding and the soil-structure interaction finite element model. Figure 12a shows that the elastic bedding model overestimates the maximum normal forces (N) by approximately 20% in the vicinity of the invert as a consequence of differences in the distribution of the loading acting on the lining (Figure 10). However, the bending moments (M) in the lining are twice the magnitude for the engineering bedding model as compared to the FE soil-structure interaction model, which evidently leads to a conservative design of the reinforcement in the linings.

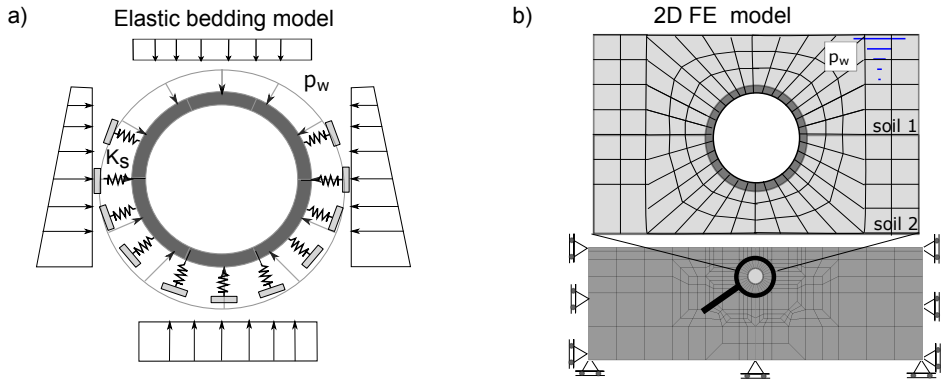

Figure 11: Finite element models for calculation of structural forces: a) elastic bedding model b) 2D model of soil-structure interaction.

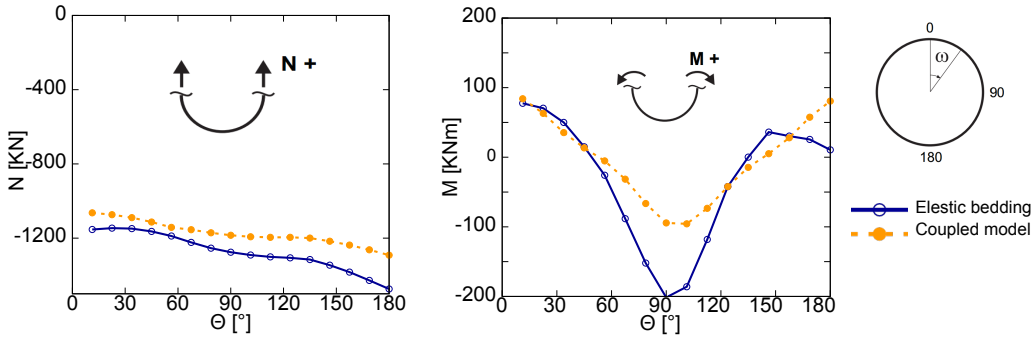

Figure 12: Normal forces (left) and bending moments (right) from the elastic bedding finite element model and the 2D soil-structure finite element model according to Figure 11.

3. Process-oriented 3D FE simulation for evaluation of time-variant loading on linings during tunnel construction

The surface-to-surface contact between the interacting surfaces of the grouting and lining elements is applied to obtain the normal contact (earth) pressure and the water pressure acting on the lining shell during the advancement of a shield driven tunnel from computational simulations. First, in Subsection 2.4, the loading acting on the tunnel lining in steady state is compared with the in situ loadings obtained by means of analytical solutions. Subsequently, Subsection 3.1 contains results from a parametric study conducted to evaluate the magnitude and the change of the pressure acting on the lining for different magnitudes and gradients of the

grouting pressure, permeabilities of the soil and time-dependent properties of the grouting mortar during a tunnel advance in soft, water saturated soils. To this end, a simulation model based on project data of the Wehrhahn line metro in Düsseldorf (20) is employed.

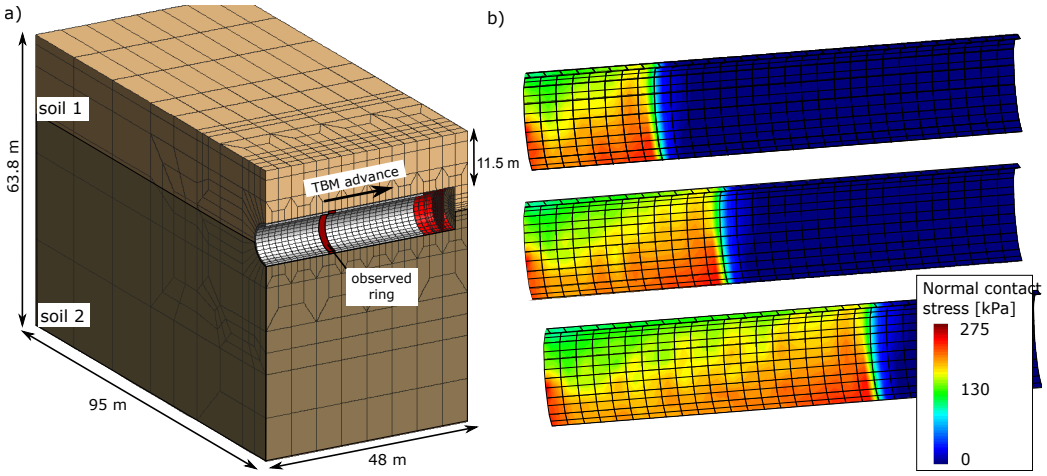

Figure 13: Simulation model for evaluation of loading on lining: a) Geometry and finite element discretization of the model; b) example for computed normal contact stresses acting on the lining evolving in time.

The geometry of the tunnel and the section of the soil considered in the simulations as well as the finite element discretization is illustrated in Figure 13. The subsoil consists of two soil layers: low terrace of the river Rhine with sand and gravel of the quaternary (16.2 m thickness); tertiary with slightly silty and medium sandy to silty fine sand (47.5 m thickness). The tunnel is excavated under an overburden of 11.5 m.

The water saturated soil is discretized by 27-node hexahedral two-phase finite elements with a quadratic approximation of the displacements and linear approximations of the liquid pressure. In this model, the shield machine, the hydraulic jacks and the segmented lining are considered as separate components. The TBM has a cutting wheel of 9.475 m diameter and a length of 9.42 m with slightly tapered geometry while the lining has a circular shape with a outer diameter of 4.60 m and a thickness of 0.45 m. The lining is modeled using kinematic linear elements, while the TBM is discretized using kinematic nonlinear Total Lagrangian hexahedral elements, both with a quadratic approximation of the displacements. The gap between the excavated soil boundary and the lining with a width of 0.145 m, evolving behind the shield machine, is filled with the grouting

material, modeled by installation of the two-phase grouting elements and considering the solidification behavior as described in Section 2.2.1. It should be noted, that due to stress-free installation, the actual size of the gap, which is filled with the pressurized fluid, depends on the deformation of the soil. All parameters used in the numerical analysis are summarized in Table 1. The model contains 6328 finite elements and 125647 degrees of freedom. For the assessment of the quality of the numerical solution in terms of spatial and temporal discretization we refer to Appendix 6.2.

The simulated tunnel advance consists of 32 excavation steps of 1.5 m length each. In the initial step, the shield with a length of 9.42 m is embedded in the soil for 8 steps, with the first two lining rings and one grouting ring installed behind the TBM. Subsequently, the stepwise TBM advance, the soil excavation and the installation of the lining and grouting elements with corresponding boundary conditions, is performed within 24 steps.The in situ stresses in the soil due to gravity are imposed, where the magnitude of the horizontal earth pressures is determined by means of the coefficient $K_0 = \frac{\nu}{1-\nu}$. In the simulation of the stepwise excavation, the contact condition between the grouting and the lining interacting surfaces is simultaneously activated. The shield machine is thrust forward in five successive advancement steps of 0.3 m and 360 seconds each. After the advancement of the TBM, the lining and grouting rings are installed, the heading and grouting pressures are applied. During the stillstand period (1800 s), the consolidation process is considered by applying time increments in 10 successive steps, adopting a logarithmic distribution of time intervals. The face support pressure is prescribed as 150 kPa at the tunnel axis, with a linear gradient of 10 kPa/m over the height.

In the following simulation scenarios, the influence of the grouting pressure, the gradient of grouting pressure, the soil permeability and the effect of time-dependent properties of grouting material is investigated. These parameters are defined for each set of simulations, while the other material properties of the model components are adopted according to Table 1. The normal pressure t_N acting on the tunnel lining in different construction stages according to the simulation model is visualized on the right hand side of Figure 13.

3.1. Influence of the magnitude of grouting pressure

In this subsection, the influence of the magnitude of the grouting pressure on the spatio-temporal evolution of the loading of the lining shell is investigated. The level of the grouting pressure is prescribed at discrete locations along the front face of the finite elements representing the tail void gap. Two scenarios are investigated: p_g = 150 kPa, which approximately corresponds to the hydrostatic

Parameters	Soil 1	Soil 2	Lining	Grout	Machine
Model	DP	DP	LE	GM	LE
Young's Modulus — E [MPa]	50	100	30000	50	210000
Hardening modulus — [MPa]	14.5	39	-	-	-
Poisson ratio — ν [-]	0.25	0.25	0.2	0.45	0.15
Density — ρ [Kg/m^3]	1732.0	2038	2500	2000	7600
Porosity [-]	0.2	0.2	-	0.2	-
Cohesion [kPa]	75	75	-	-	-
Friction angle — φ [°]	30	35	-	-	-
Permeability [m/s]	$10^{-6(-4,-8)}$	$10^{-6(-4,-8)}$	-	0.0001	-
Stiffness ratio— $E^{(1)}/E^{(28)}$ [$-$]	-	-	-	0.6	-
Hydration time— t_E [h]	-	-	-	8	-
Hydration parameter— t_E [h]	-	-	-	6(4)	-

DP:elastoplastic Drucker-Prager model; LE: Linear elastic model; GM: Aging grouting mortar model

Table 1: Material parameters used in the simulation model.

water pressure at the centroid of the tunnel cross section (Figure 14) and p_g = 300 kPa, which represents a level significantly larger than the hydrostatic water pressure (Figure 15). The gradient of the pressure remains constant at 10 kPa/m. The permeability of both soil layers is assumed as k_s=10^{-6} m/s.

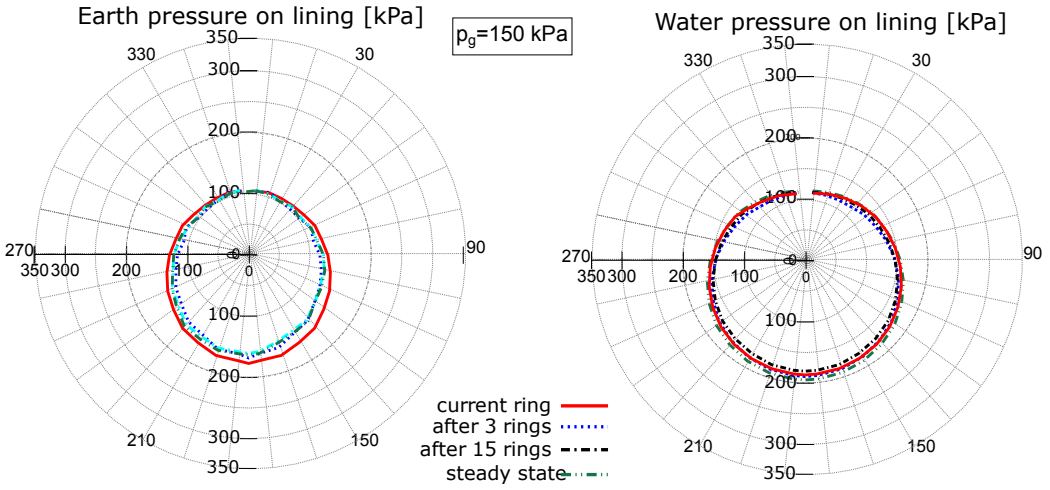

Figure 14: Spatio-temporal evolution of the earth pressure and the water pressure acting on the tunnel lining for a low grouting pressure (p_g=150 kPa).

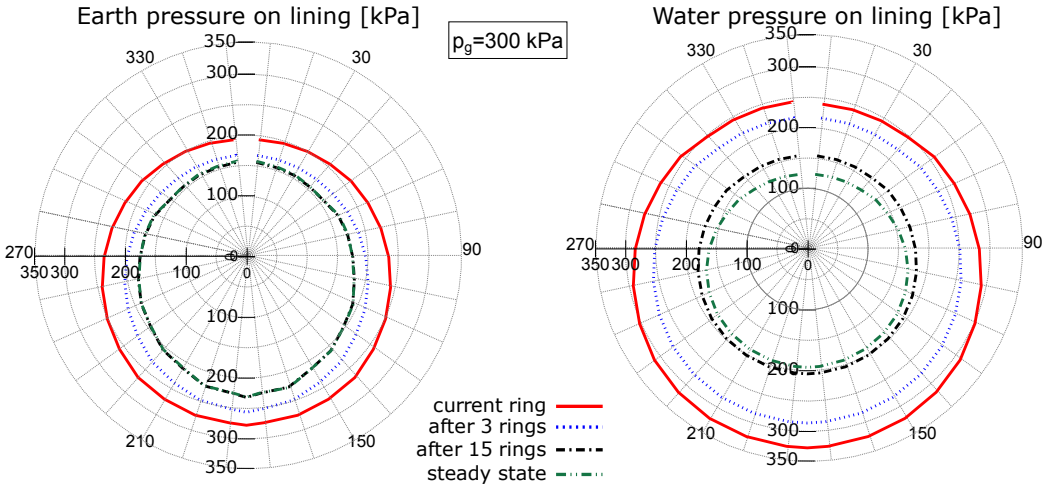

Figure 15: Spatio-temporal evolution of the earth and the water pressure acting on the tunnel lining for a high grouting pressure (p_g=300 kPa).

For the lower value of the grouting pressure (p_g=150 kPa), the resulting earth pressure on the tunnel does not change significantly in time since the gradient of the applied averaged grouting pressure and the hydrostatic water pressure - constituting the driving force for the infiltration of grouting water into the soil - is small. As a relatively high soil permeability of k_s=10^{-6} m/s is assumed, the change of water pressure dissipates quickly to a steady state.

In the second scenario, where an average grouting pressure of 300 kPa with a gradient of 10 kPa is applied, the resulting earth pressure and the temporal change are considerably larger than in the first example. The water pressure dissipates from the applied level of the grouting pressure to the hydrostatic stress state. While the water pressure in both cases converges to the hydrostatic state, the final (steady state) total earth pressure acting on the tunnel lining is larger if the applied grouting pressure is larger and does not converge to the in situ earth pressure as is generally assumed. This implies that the loading history plays a role in the temporal evolution of the loadings acting on the lining! This effect, which is caused by the change of the stiffness of the grouting in time is associated with the "freezing" of deformations. This will be further investigated in Subsection 3.2.

Figure 16 contains the distribution of the normal forces (N) and bending moments (M) for both investigated grouting pressures (p_g= 150 and 300 kPa) at steady state. As expected, the induced normal forces are much higher for high grouting pressure. While for the larger grouting pressure the distribution of the

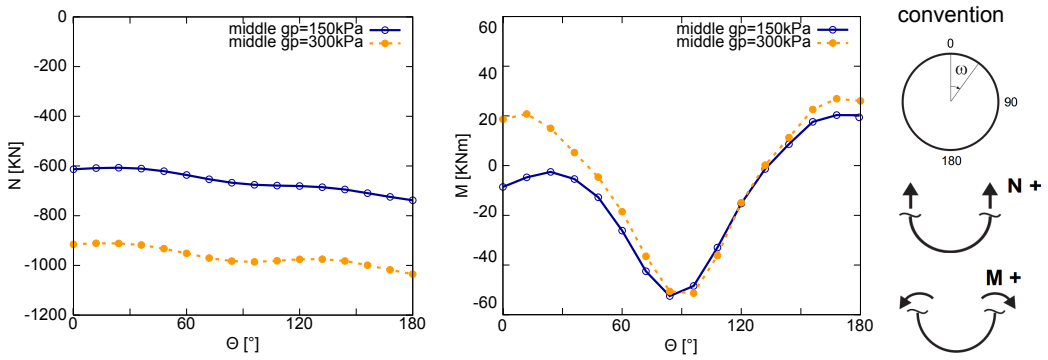

Figure 16: Long term normal forces and bending moments in the tunnel lining at steady state for two different levels of the grouting pressure.

bending moments is more or less symmetric, a more asymmetric distribution with a smaller moment recorded at the tunnel crown is obtained from the analysis with p_g= 150 kPa.

3.2. Influence of the grouting pressure distribution

Since the previous study has shown, that the initial grouting pressure has an effect on the final loading on the lining after consolidation processes have reached a steady state, we further investigate the question on the "memory effect" of the pressure transferred to the lining via the stiffening grouting material. To this end, the evolution of the earth and water pressure in time is evaluated for a grouting pressure at the tunnel axis p_g = 300 kPa, adopting, two scenarios for the pressure gradient over the height of the tunnel. One case refers to a positive gradient of 15 kPa/m (Figure 17 left, Figure 18 left) while in the second scenario a negative (non-physical) gradient of -15 kPa/m (Figure 17 right and Figure 18 right) of the grouting pressure is assumed. The soil permeability is assumed as k_s= $10^{-6}\,m/s$.

As far as the evolution of the water pressure is concerned, a comparison of the left and right hand side of Figure 18 shows, that the distribution of the water pressure strongly follows the prescribed grouting pressure boundary condition in the first step, and consequently differs significantly for a positive (left) and negative (right) gradient of the grouting pressure. However, the water pressure dissipates in time and converges to the hydrostatic stress state after three days, independent of the initially prescribed grouting pressure conditions.

Figure 17 contains the evolution of the earth pressure acting on the tunnel lining for the two grouting pressure scenarios (positive gradient in Figure 17 left and negative pressure gradient in Figure 17 right). Immediately after grouting,

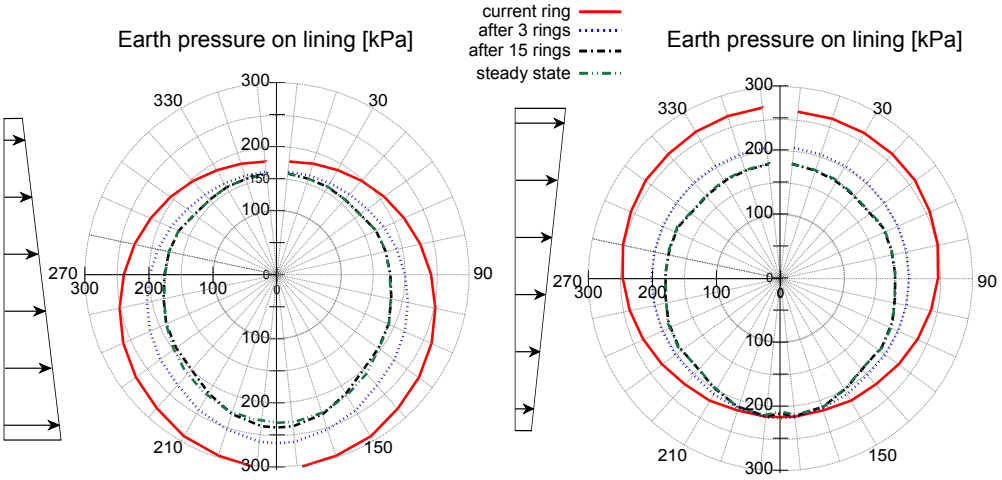

Figure 17: Spatio-temporal evolution of the earth pressure acting on the tunnel lining for two different distributions of the applied grouting pressure: Left: grouting pressure gradient 15 kPa/m; right: grouting pressure gradient -15 kPa/m.

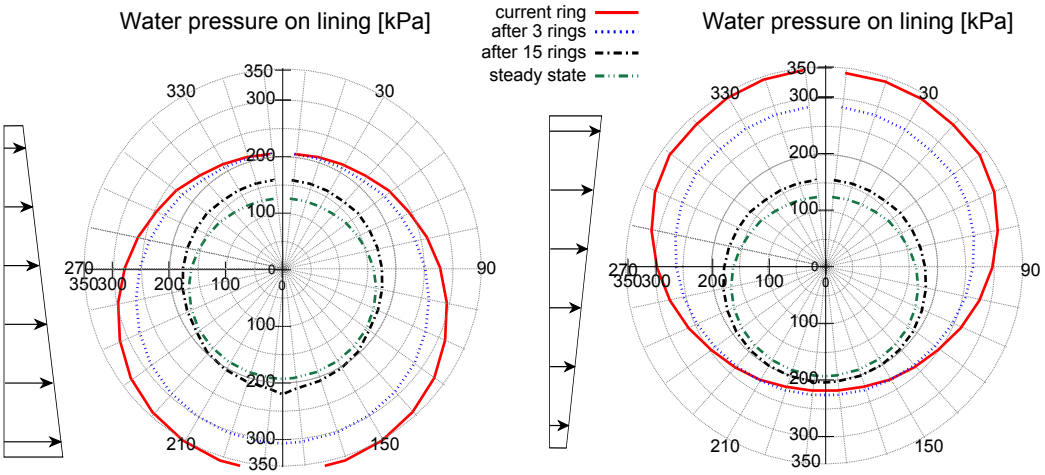

Figure 18: Spatio-temporal evolution of the water pressure acting on the tunnel lining for two different distributions of the applied grouting pressure: Left: grouting pressure gradient 15 kPa/m; right: grouting pressure gradient of -15 kPa/m.

the loading distribution is, similar to the water pressure, significantly affected by the applied grouting pressure conditions. Interestingly, however, while also dissipating in time, the (total) earth pressure does not converge to the same value even when the consolidation and infiltration processes in the soil and the grouting

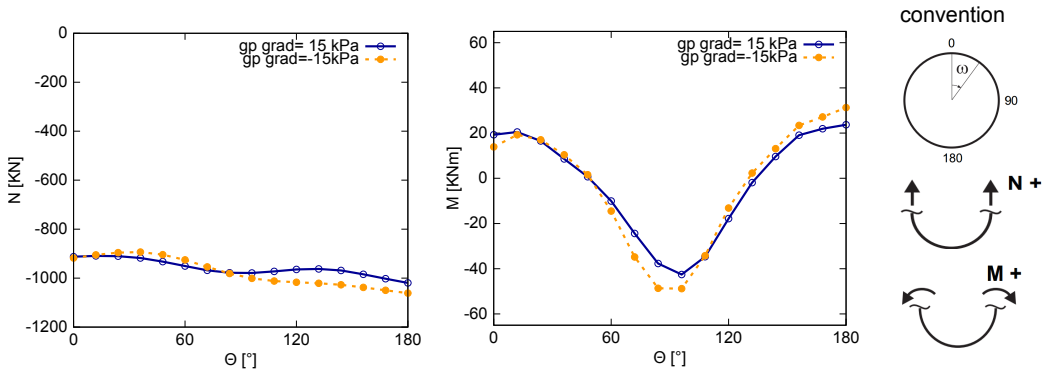

Figure 19: Normal forces and bending moments in tunnel lining for the final stage of the loading for two gradients of the grouting pressure (p_g= 15 and -15 kPa).

mortar have reached a steady state! Following the distribution of the loading, one obtains the difference in structural forces in the lining for the steady state in Figure 19.

This is a consequence of the effect of the loading history on the time variant stiffening of the grouting mortar and the stress distribution in the soil. The material solidification of the grouting mortar is connected, according to Subsection 2.2.1, with aging induced strains. These strains evolve in time and contain information on the complete loading process. Since a coupled hydro-mechanical is employed, the interaction between the grouting pressure and the ground water is implicitly considered, and the history of both mechanical as well as hydraulic processes have an influence on the final loading of the tunnel shell. A different loading history in these two examples leads to strain "freezing" under different loading conditions and consequently to a different final total stress state around the lining, although the water pressures finally always dissipate to the hydrostatic stress state. The same effect is apparent in the first parametric study, where the influence of the magnitude of the grouting pressure is investigated (see Subsection 3.1).

3.3. Influence of soil permeability

In the second parametric study, the influence of the soil permeability on the distribution of the loading on linings in different construction phases is investigated. The grouting pressure is assumed as g_p = 300 kPa at the tunnel axis with a gradient of linear change of 10 kPa/m in both cases. Two different soil permeabilities are considered: k_s=$10^{-4}\,m/s$, denoted as high permeability soil (Figure 20) and k_s = $10^{-8}\,m/s$, denoted as low permeability soil (Figure 21), respectively.

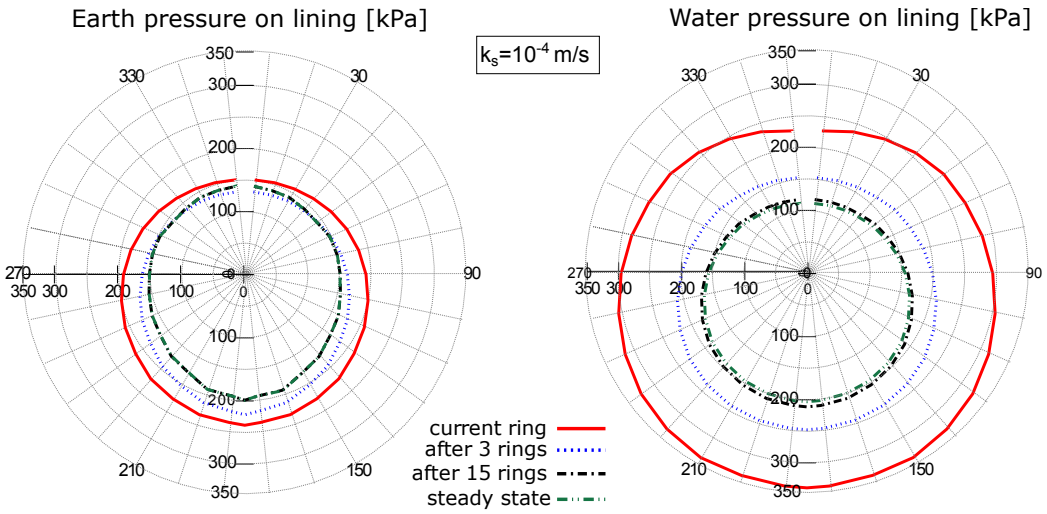

Figure 20: Spatio-temporal evolution of the earth and water pressure acting on the tunnel lining for highly permeable soil (k_s=10^{-4} m/s).

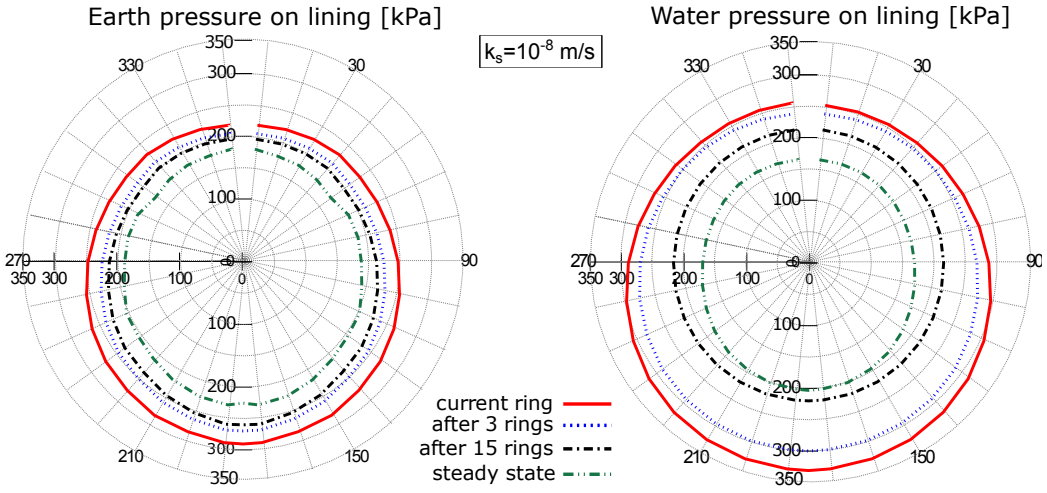

Figure 21: Spatio-temporal evolution of the earth and water pressure acting on the tunnel lining for soil with low permeability (k_s=10^{-8} m/s).

In the case of high permeability, the water pressure dissipates almost immediately (Figure 20 right). As a consequence, the total normal pressure acting on the tunnel lining is not developed in full capacity as compared to low permeable soils, shown on the left hand side of Figures 20 and 21, respectively. This observation

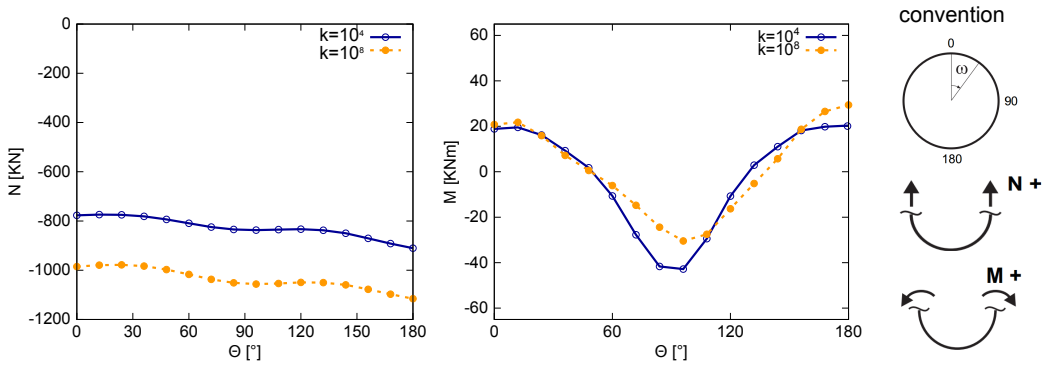

Figure 22: Long-term normal forces and bending moments in tunnel lining at steady state for two different soil permeabilities k_s.

is in agreement with (11), where it was noticed that the measured pressures were lower than predicted in the design stage for a tunnel constructed in sand.

From Figure 21 (left) it is observed, that in case of a tunnel drive in low permeable soil, the resulting earth pressure acting on the lining is significantly higher as compared to the high permeable soil conditions (see Figure 20 (left)). This refers to the early stages as well as to the long term situation at steady state.

Figure 22 shows the distribution of the normal force N and bending moment M at steady state of the two examined cases. As the loading on the lining is larger for tunneling in soils with a low permeability, also the normal forces are considerably larger as compared to soils with low permeability. However, slightly larger bending moments are observed for the case of high soil permeability due to the larger influence of the earth pressure as compared to the grouting pressure, connected with a larger ovalization of the tunnel structure.

3.4. Effect of time dependent properties of the grouting material

The fourth study investigates the influence of the stiffening characteristics of the grouting material on the temporal evolution of the spatial distribution of the loadings acting on the lining. The grouting pressure at the tunnel axis is assumed as p_g=300 kPa , with a gradient of 10 kPa/m over the height, and a soil permeability of k_s=$10^{-6}\,m/s$. Two cases are analyzed: In one simulation, the properties of the grouting material are considered as time-dependent with the same parameters as assumed previously in Section 3.1; In a second case, the grouting was modeled as a fully saturated porous material, with a constant elastic stiffness $E = 0.5\,MPa$ and a permeability of k_g=$10^{-6}\,m/s$.

The temporal evolution of the earth pressure acting on the lining according to a tunnel advancement simulation is plotted for the initial, intermediate and stationary state in Figure 23 (left) for time-dependent grouting material properties and for time-independent properties in Figure 23 (right).

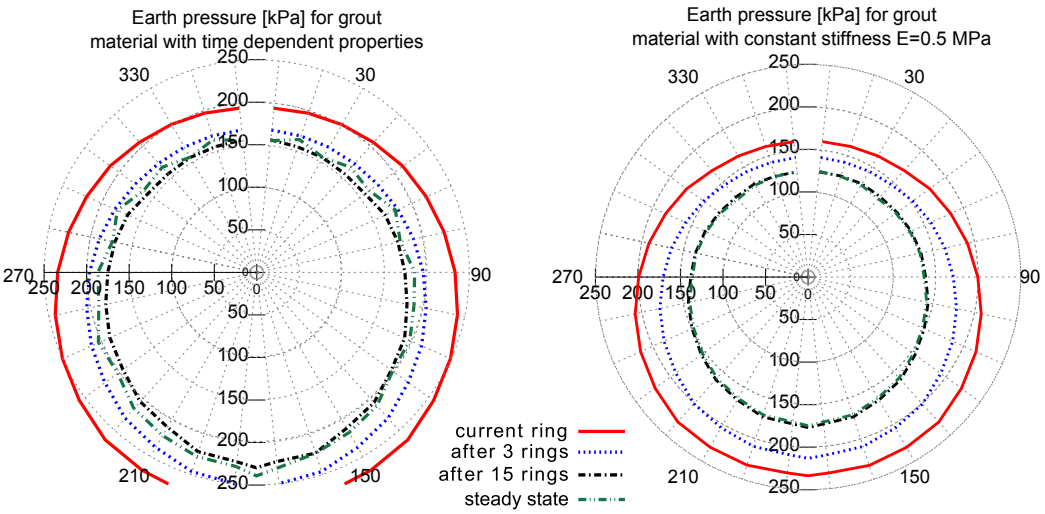

Figure 23: Spatio-temporal evolution of the earth pressure acting on the lining for two different models of the grout material: left – solidification model according to Subsection 2.2.1; right – constant grout stiffness E_g=0.5 MPa.

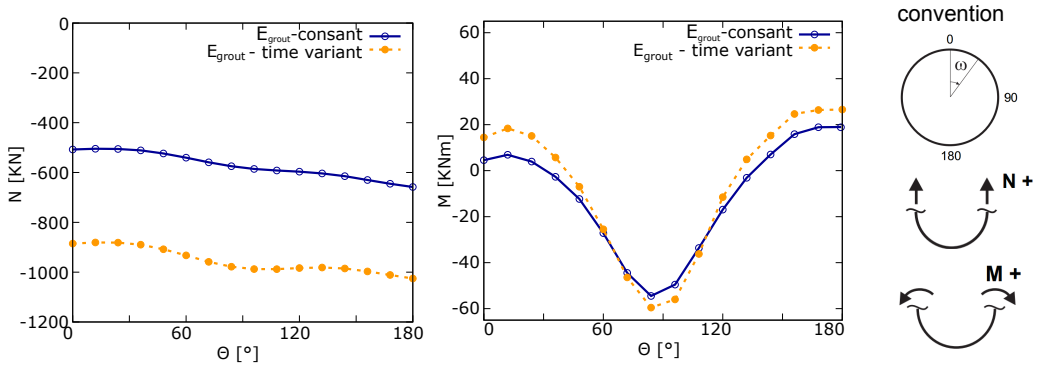

Figure 24: Long term normal forces and bending moments in tunnel lining at steady state for two different models of the grout material (constant and time-variant elastic stiffness E_g).

Comparing the two results, it becomes apparent that consideration of the time dependent characteristics in the numerical model plays an important role and leads

to considerably different distribution of the loadings acting on the tunnel lining during the different construction phases as well as for the steady state. The grouting model, when considering a time-dependent stiffness of the grouting material (see Section 2.2), represents a quasi-fluid state in the initial state after applying the grouting pressure. In the initial step, the stiffness of the grouting material with time-dependent properties is approximately 5×10^3 times smaller as compared to the material with a constant Young's modulus. This allows for the pressurization of the tail gap grouting in full capacity, leading to higher total normal stresses acting on the tunnel lining. For the detail explanation of the mechanisms evolving, we refer to the Appendix 6.

Figure 24 shows the consequences of the different loading distributions obtained from the two scenarios for the grouting mortar on the distribution of the structural forces in the lining structure. Considerably larger normal forces are recorded for the time-variant material properties of the grouting mortar as compared to the assumption of a constant stiffness.

4. Effect of interface properties between the lining shell and the tail void grouting

In Subsection 2.3 the interface between the lining and the grouting was defined such that only the normal contact pressure t_N is transferred through the contact interface. This assumption is motivated by the fact that at the moment of grouting injection, the grout material has fluid-like and therefore does not transfer shear forces. As shown in the previous Section, the maximum magnitude of the pressures acting on the lining shell is observed immediately after the application of the tail gap grouting, when the material is still in a liquid state, and therefore, the previous assumption is valid in early stages of the construction process. It is also supported by the German recommendations for the design of segments linings (29). However, during hydration of the grouting mortar and infiltration of the pore water, the material stiffens and a bond between the grouting and lining material establishes gradually.

To obtain an insight on role of the transfer of tangential forces between the grout and the lining along the outside face of the tunnel shell, we now assume a full bond between the lining and the grout in the numerical simulations documented in this Section and compare the obtained results with the case of a frictionless interface. To this end, a tying condition is introduced by means of the LAGRANGE multipliers method to enable the evaluation of tangential reaction forces acting along the lining structure.

4.1. Tying between lining and grouting along the grout-lining interface

The tying constraint between the grouting and lining elements along their interface is accomplished by means of the LAGRANGE multiplier method. The constraints are imposed between the outer lining surface, denoted as the "slave surface" and the inner grouting surface, denoted as the "master surface" (see Figure 25a). The contact constraints are fulfilled at each quadrature point on the so-called slave contact surface.

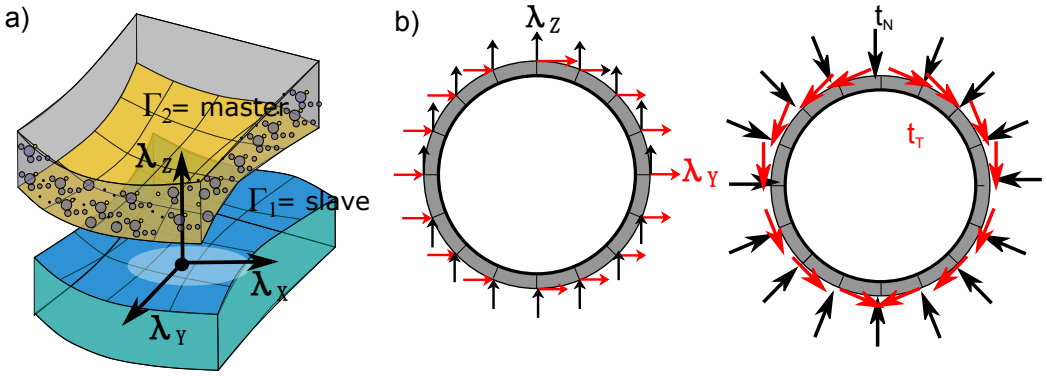

Figure 25: a) Tying constraint between lining and grouting interface and resulting LAGRANGE multipliers ; b) Transformation to traction forces in polar coordinates—normal forces and tangential forces.

The LAGRANGE multiplier method (32) introduces a vector of additional unknowns λ, the so-called discrete LAGRANGE multipliers corresponding to the number of constraints (*noc*). Adding the constraints $G(u^{1,2})$ in the total potential $\Pi(u^{1,2})$ results in the following extended potential $\Pi_{LM}(u^{1,2})$:

$$\Pi_{LM}(u^{1,2},\lambda) = \Pi(u^{1,2}) + \sum_{j}^{noc} \lambda_j G_j(u^{1,2}) \tag{19}$$

The solution of Eqn. 19 constitutes a saddle point of the extended potential Π_{LM}, i.e. the solution is a maximum of Π_{LM} with respect to the LAGRANGE multipliers λ and a minimum with respect to the displacements u (27). In the framework of the finite element method, the linearized form of the variational problem is given as:

$$\begin{bmatrix} \mathbf{K}_{LM}^{u^{1,2}} + \mathbf{K}_{LM}^{\lambda} & C^T \\ C & 0 \end{bmatrix} \cdot \begin{bmatrix} \delta\mathbf{u}^{1,2} \\ \delta\lambda \end{bmatrix} = \begin{bmatrix} -\mathbf{r}_{LM}^{u^{1,2}} \\ -\mathbf{r}_{LM}^{\lambda} \end{bmatrix}, \tag{20}$$

with the internal force vectors

$$\mathbf{r}_{LM}^{u^{1,2}} = \frac{\partial \Pi_{LM}}{\partial u} \qquad \text{and} \qquad \mathbf{r}_{LM}^{\lambda} = G(u)\,, \tag{21}$$

and the components of the global system matrix given as:

$$\mathbf{K}_{LM}^{u^{1,2}} = \frac{\partial^2 \Pi(u)}{\partial u^2}, \qquad \mathbf{K}_{LM}^{\lambda} = \sum_{j}^{noc} \lambda_j \frac{\partial^2 G_j(u)}{\partial u^2} \qquad \text{and} \qquad C = \frac{\partial G_j(u)}{\partial u}\,. \tag{22}$$

The Lagrange multipliers λ_j are equivalent to the reaction force between two constrained surfaces (Figure 25b), and therefore can be directly used as a measure of the loadings acting on the tunnel lining after transformation to a polar coordinate system to obtain the normal pressure (t_N) and the tangential traction forces (t_T).

4.2. Influence of the interface condition on the distribution of the loadings on tunnel lining in steady state conditions

In this subsection, the loadings acting on the lining structure in the final state i.e. after consolidation processes have reached a steady state, are compared for frictionless and fully bonded interface conditions (see Subsections 2.3 and 4.1).

The first example is related to the 2D analysis of the soil-tunnel interaction in steady state conditions as described in Subsection 2.4 without consideration of a time-dependent grout material and the construction process (see Figure 26).

Figure 26b compares the normal and tangential loadings transferred along a fully bonded interface (dotted lines) with the normal pressure transferred along a frictionless interface (line with squares). One observes, that non-negligible shear loadings (t_T) are transferred to the lining shell in case of a fully bonded interface, which also affects the distribution of the normal loading (t_N).

Next, the scenarios investigated previously in Section 3 for a frictionless lining-grout interface in the context of 3D simulations of the staged tunnel construction process, taking into account all time-dependent processes such as step-wise TBM advance and construction of lining shell, consolidation of the soil and time dependent stiffening of the grout, are now re-analyzed for the case of a fully bonded lining-grout interface. The results for the frictionless and the fully bonded case are compared for the steady state for different assumptions concerning the grouting pressure (analogous to Subsection 3.1), the grouting pressure gradient over the height (analogous to Subsection 3.2), the soil permeability (analogous to Subsection 3.3) and the time (in)dependent grouting properties (analogous to Subsection 3.4).

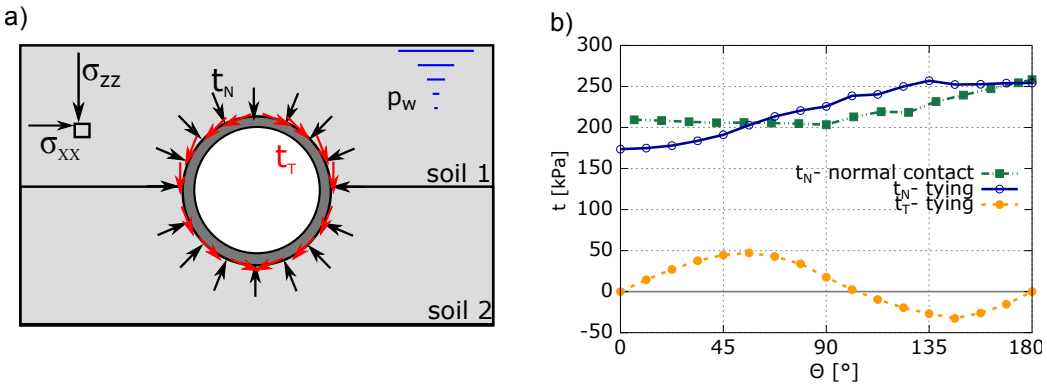

Figure 26: Influence of interface conditions on the loading on linings for a 2D steady state analysis: a) Tying constraint between lining and grouting interface; b) Comparison between frictionless conditions (normal contact) and fully bonded conditions (tying).

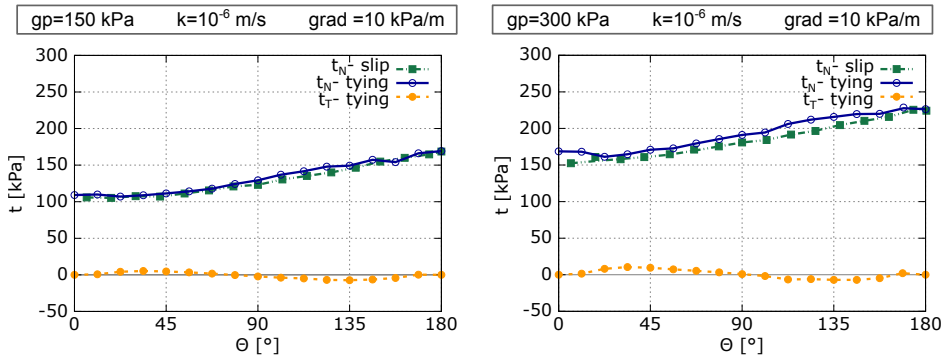

Figure 27: Comparison between frictionless conditions (normal contact) and fully bonded conditions (tying) for two levels of the average grouting pressure (p_g= 150 kPa and 300 kPa (see Subsection 3.1)).

Figure 27 shows the results from advancement simulations for two different levels of the grouting pressure (p_g= 150 kPa and 300 kPa) for frictionless and fully bonded interface conditions. For both pressure levels, only a marginal difference between the results for the normal pressure (t_N) acting on the lining is observed. Also, the tangential forces (t_T) induced in the fully bonded case are negligible.

When comparing the results for two different gradients of the applied grouting pressure over the height, again the influence of the interface conditions is marginal (see Figure 28).

Similar, a negligible effect of the interface properties is obtained from the numerical simulations assuming two values of the soil permeability (k_s=10^{-4} and

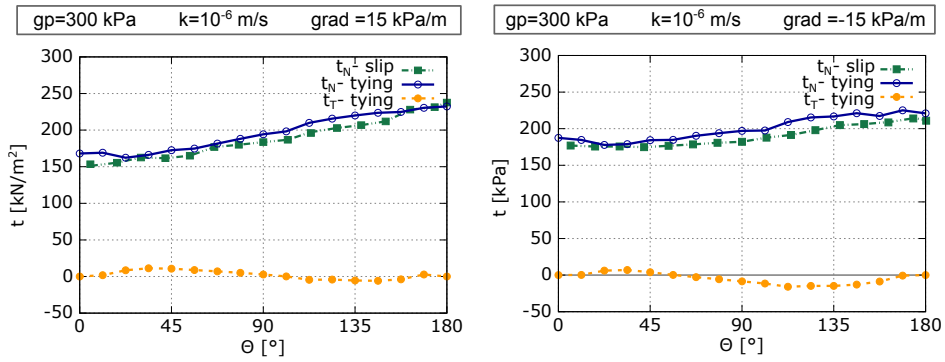

Figure 28: Comparison between frictionless conditions (normal contact) and fully bonded conditions (tying) for two gradients of the grouting pressure over the height (dp_g/dz= 15 kPa/m and -15 kPa/m (see Subsection 3.2)).

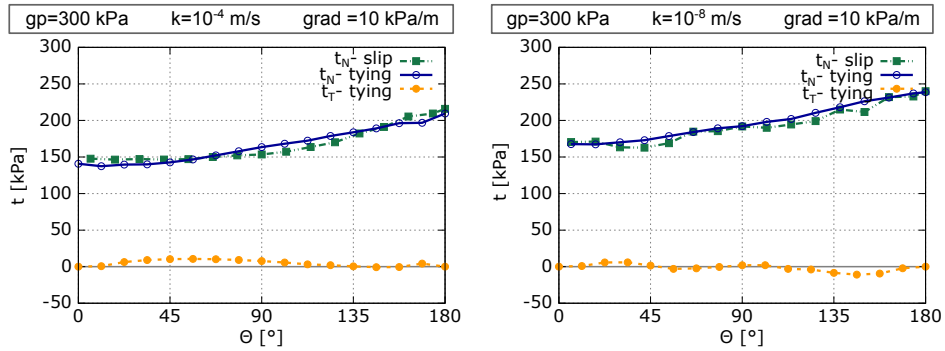

Figure 29: Comparison between frictionless conditions (normal contact) and fully bonded conditions (tying) for two soil permeabilities (k_s=10^4 m/s and k_s= 10^8 m/s (see Subsection 3.3)).

10^{-8} m/s (see Figure 29).

Figure 30 shows the results from advancement simulations assuming a constant (non-physical, time-independent) elastic stiffness of the grouting material (E_g=0.5 MPa). In this case, the influence of the interface conditions on the distribution of the normal pressure (t_N) is more pronounced as compared to the previous scenarios. Obviously, if the evolution of inelastic aging induced strains ε^t of the grouting material is not considered and consequently the grouting stiffness is significantly larger during the installation stage, the loading induced on the lining becomes more dependent on interface properties.

Figure 31 summarizes the final normal pressure loadings acting on the lining of the tunnel after all consolidation processes have reached a steady state obtained

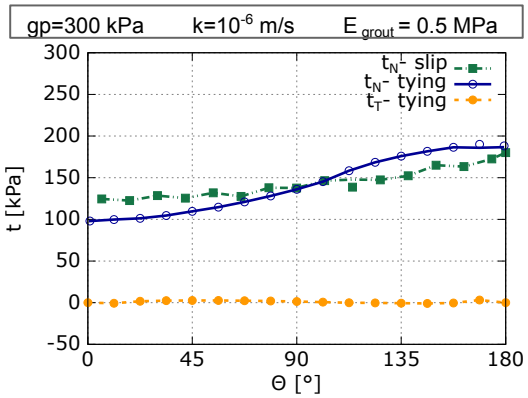

Figure 30: Comparison between frictionless conditions (normal contact) and fully bonded conditions (tying) assuming a constant (time-independent) elastic stiffness of the grouting material (E_g=0.5 MPa (see Subsection 3.4)).

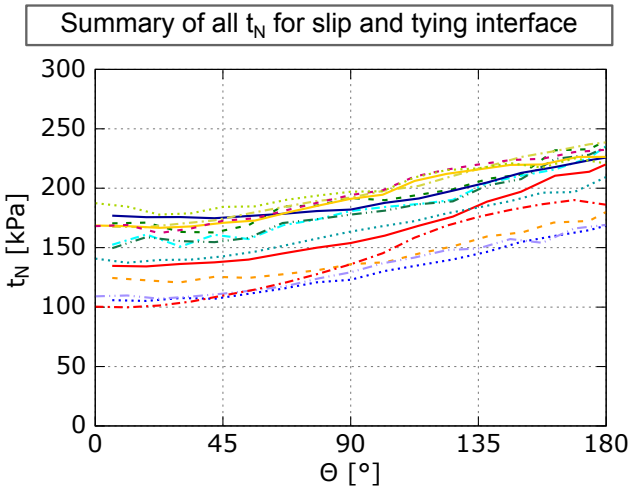

Figure 31: Range of the normal pressure (t_N) acting on the tunnel lining obtained from all scenarios investigated in Subsection 4.2.

from all scenarios investigated in this Subsection. This figure shows, that the loading on lining in the steady state does not necessarily converge to the in situ state, but strongly depends on the hydraulic soil properties and the applied support measures. For the specific tunnel example used as the basis for this comparative analysis, a difference of $\approx$ 75 kPa between the minimum and maximum normal lining pressure is recorded in Figure 31.

5. Conclusions

In the paper selected factors influencing the spatial and temporal evolution of the loadings on the tunnel lining during mechanized tunnel construction have been analyzed numerically. It attempts to provide an answer to the question, if the loadings acting on the lining, after the consolidation process has reached a steady state, is eventually only controlled by the in situ earth pressure, how this loading evolves in time and to which extent it depends on grouting pressure, the soil permeability and the evolution of the grouting stiffness.

To this end, a process-oriented 3D finite element model for the numerical simulation of the tunnel advancement process in mechanized tunneling, which accounts for the stepwise advancement of TBM, ring-wise installation of the lining structure and the filling of the tail void by a pressurized (solidifying) grouting material, whose stiffness and permeability evolve with time, as well as for soil consolidation, is employed. The consideration of all relevant time dependent effects and their interactions in a simulation model for mechanized tunneling is the prerequisite to obtain reliable data on the temporal evolution and spatial distribution of surface forces acting on the lining in various construction phases and in the final state.

For the accurate extraction of the traction forces acting along the interface between the lining shell and the grouting material, a contact formulation was employed. In addition to frictionless interface conditions, also a fully bonded state was considered by applying tangential constraints by means of the Lagrange multiplier method.

From a comparison of results of tunnel advance simulation with frictionless and with fully bonded interface conditions, it was found, that after reaching a steady state of the consolidation and hydration processes in the soil and the grouting, only a marginal influence on the distribution of the loading on the lining was found. Hence, it is concluded, that the tangential (frictional) forces along the tunnel lining may be neglected.

However, it was shown that the loading acting on the tunnel lining depends, besides on the (in situ) earth and the water pressure, strongly on the grouting pressure initially applied at the shield tail to fill the tail gap after the installation of a new ring. Besides the magnitude of the pressure at the tunnel axis, also the spatial distribution (i.e. the gradient) of the grouting pressure has an influence on the final distribution of the normal pressure acting on the tunnel lining. Furthermore, a considerable dependence of the loadings acting on the tunnel lining on the permeability of the soil was observed in comparative computational simulations of

different scenarios both during construction as well as in the final state, after the soil consolidation has reached a steady state.

It is therefore concluded, that the final state of loadings acting on tunnel linings is not only controlled by the in situ state and the water pressure in the soil but also by the grouting process, the stiffening characteristics of the grouting mortar and the hydraulic properties of the surrounding soil. The stiffening of the grouting materials is connected with aging induced (permanent) strains and related "frozen" deformations, which depend on the loading history. Since a coupled hydro-mechanical model is employed, the interaction between the grouting pressure and the ground water is implicitly considered, and therefore the history of both mechanical and hydraulic processes have an influence on the final loading of the tunnel shell. Hence, different loading conditions (such as the initial grouting pressure or different infiltration times from the annular gap into the soil), although the water pressures finally always dissipates to the hydrostatic stress state in the soil, lead to different final states of effective stresses around the lining and, consequently, to different total normal loadings acting on the tunnel lining.

The finding, that the loadings acting on tunnel linings in the steady state may differ significantly from the in situ state has consequences for tunneling engineering, as currently the in situ earth pressure is used as the basis for engineering analysis and design of tunnel linings.

Acknowledgement

Financial support for this work was provided by the German Science Foundation (DFG) in the framework of project C1 of the Collaborative Research Center SFB 837. This support is gratefully acknowledged.

[1] Alsahly, A., Stascheit, J., Meschke, G.: Advanced finite element modeling of excavation and advancement processes in mechanized tunneling. Advances in Engineering Software **100**, 198 - 214 (2016).

[2] Augarde, C., Burd, H.: Three-dimensional finite element analysis of lined tunnels. International Journal for Numerical and Analytical Methods in Geomechanics **25**, 243–262 (2001)

[3] Bezuijen, A., Talmon, A.: Tunnelling. A Decade of Progress. GeoDelft 1995-2005, Chapter: Grout pressures around a tunnel lining, influence of grout consolidation and loading on lining, pp. 109 –114. Taylor & Francis (2006)

[4] Bezuijen, A., Talmon, A., Kaalberg, F., Plugge, R.: Tunnelling. A Decade of Progress. GeoDelft 1995-2005, Chapter: Field Measurement of Grout Pressure during Tunnelling of the Sophia Rail Tunnel, pp. 83–93. Taylor & Francis, London (2006)

[5] Blom, C.: Design philosophy of concrete linings for tunnels in soft soils. Ph.D. thesis, Delft University of Technology, The Netherlands (2002)

[6] Bouma, A.: Elasto-statics of slender structures. Ph.D. thesis, Delft University of Technology, The Netherlands (1993)

[7] Dadvand, P., Rossi, R., Oñate, E.: An object-oriented environment for developing finite element codes for multi-disciplinary applications. Archives of Computational Methods in Engineering **17**, 253–297 (2010)

[8] Do, N., Dias, D., Oreste, P., Djeran-Maigre, I.: A new numerical approach to the hyperstatic reaction method for segmental tunnel linings. International Journal for Numerical and Analytical Methods in Geomechanics **38**(15), 1617–1632 (2014)

[9] Duddeck, H., Erdmann, J.: On structural design models for tunnels in soft soil. Underground Space **9**, 246–259 (1985)

[10] El-Nahhas, F., El-Kadi, F., Ahmed, A.: Interaction of tunnel linings and soft ground. Tunnelling and Underground Space Technology **7**(1), 33–43 (1992)

[11] Hashimoto, T., Nagaya, J., Konda, T., Tamura, T.: Observation of lining pressure due to shield tunneling. In: R. Kastner, F. Emeriault, D. Dias, A. Guilloux (eds.) Geotechnical Aspects of Underground Construction in Soft Ground, pp. 119–124. Lyon (2002)

[12] H.Takano, Y.: Guidelines for the design of shield tunnel lining. Tunnelling and Underground Space Technology **15**(3), 303 – 331 (2000)

[13] Hudoba, I.: Contribution to static analysis of load-bearing concrete tunnel lining built by shield-driven technology. Tunnelling and Underground Space Technology **12**(1), 55–58 (1997)

[14] Kim, H., Eisenstein, Z.: Prediction of tunnel lining loads using correction factors. Engineering Geology **86**(3), 302–312 (2006)

[15] Klappers, C., Grübl, F., Ostermeier, B.: Structural analyses of segmental lining- coupled beam and spring analyses versus 3D FEM calculations with shell elements. Tunneling and Underground Space Technology **21**, 254–255 (2006)

[16] Kolymbas, D.: Geotechnik - Tunnelbau und Tunnelmechanik. Springer (1998)

[17] Koyama, Y.: Present status and technology of shield tunneling method in Japan. Tunnelling and Underground Space Technology **18**(2-3), 145–159 (2003)

[18] Laursen, T.: Computational Contact and Impact Mechanics. Springer, Berlin-Heidelberg (2002)

[19] Maidl, B., Herrenknecht, M., Maidl, U., Wehrmeyer, G.: Mechanised Shield Tunnelling. Ernst und Sohn (2012)

[20] Meschke, G., Freitag, S., Alsahly, A., Ninić, J., Schindler, S., Koch, C.: Numerische Simulation maschineller Tunnelvortriebe in innerstädtischen Gebieten im Rahmen eines Tunnelinformationsmodells. Bauingenieur **89**(11), 457–466 (2014)

[21] Meschke, G., Kropik, C., Mang, H.: Numerical analyses of tunnel linings by means of a viscoplastic material model for shotcrete. International Journal for Numerical Methods in Engineering **39**, 3145–3162 (1996)

[22] Meschke, G., Ninic, J., Stascheit, J., Alsahly, A.: Parallelized computational modeling of pile-soil interactions in mechanized tunneling. Engineering Structures **47**, 35 – 44 (2013)

[23] Morgan, H.D.: A contribution to the analysis of stress in a circular tunnel. Geotechnique **11**(1) (1961)

[24] Nagel, F.: Numerical modelling of partially saturated soil and simulation of shield supported tunnel advance. Ph.D. thesis, Ruhr University Bochum, Germany (2009)

[25] Nagel, F., Stascheit, J., Meschke, G.: Process-oriented numerical simulation of shield tunneling in soft soils. Geomechanics and Tunnelling **3**(3), 268–282 (2010)

[26] Ninić, J.: Computational strategies for predictions of the soil-structure interaction during mechanized tunneling. Ph.D. thesis, Ruhr University Bochum, Germany (2015)

[27] Popp, A.: Mortar methods for computational contact mechanics and general interface problems. Ph.D. thesis, Technische Universität München, Germany (2012)

[28] Potts, D., Zdravkovic, L.: Finite element analysis in geotechnical engineering: application. Thomas Telford Ltd (2001)

[29] Recommendations for the design, production and installation of segmental rings. DAUB (German Tunnelling Committee) working group " Lining Segment Design" (2013)

[30] Simo, J.C., Laursen, T.: An augmented lagrangian treatment of contact problems involving friction. Computers & Structures **42**(1), 97–116 (1992)

[31] Talmon, A., Bezuijen, A.: Analytical model for the beam action of a tunnel lining during construction. International Journal for Numerical and Analytical Methods in Geomechanics **37**(2), 181–200 (2013)

[32] Wriggers, P.: Computational Contact Mechanics. John Wiley & Sons (2002)

[33] Yu, H.: CASM: a unified state parameter model for clay and sand. International Journal for Numerical and Analytical Methods in Geomechanics **48**, 773–778 (1998)

[34] Verruijt, A. Soil Mechanics. Delft Academic Press. ISBN 9789065621634 (2012).

6. Appendix

6.1. Analysis of the load transfer trough grouting elements

The contact formulation developed for the computation of surface forces acting on the tunnel lining is verified by means of two benchmark tests. In the first test illustrated in Figure 32, the transfer of the load from the top surface through a rigid body to the bottom contact surface for a purely mechanical case is analyzed. The geometry and finite element mesh of the benchmark test are presented in Figure 32a, the DIRICHLET boundary conditions are depicted in Figure 32b, and the

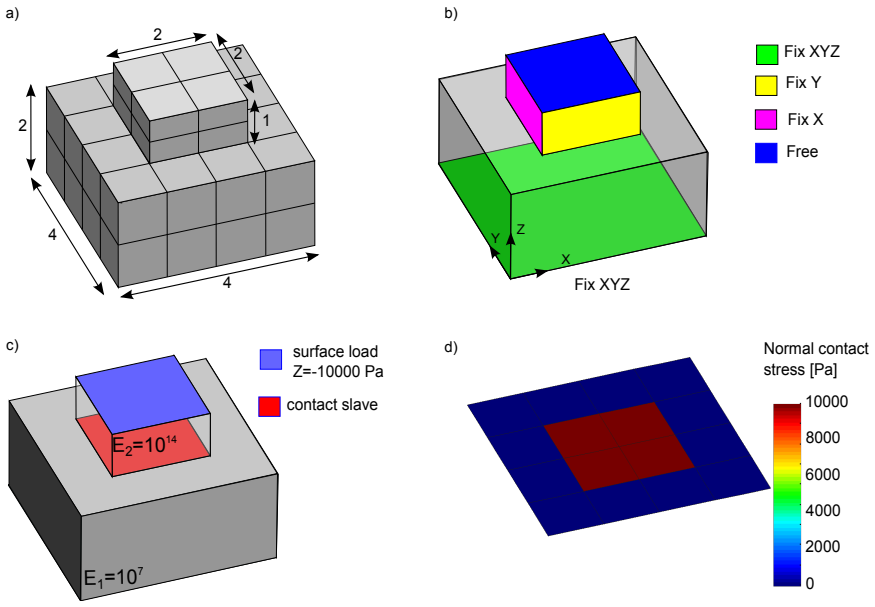

Figure 32: Verification of the contact model for a purely mechanical problem – load transfer through a stiff body to the lining (slave contact) surface: a) Finite element mesh of the benchmark example; b) boundary conditions of the model; c) loading (surface load of $-10\,\mathrm{kPa}$) and contact condition; d) normal contact force acting on the slave surface.

NEUMANN boundary conditions, i.e. the load on the top surface of the (grouting) element as well as the contact condition on the bottom surface of the element are shown in Figure 32c. The top element has a large stiffness (E_2=$10^{14}\,\mathrm{N/m^2}$) in comparison to the support element (E_1=$10^7\,\mathrm{N/m^2}$). In this test, the body experiences rigid motion due to the acting loads, which enables a full transfer of the force applied on top to the bottom face, where the contact condition is applied. Figure 32d shows the normal contact force, which, as expected, is identical to the applied force on the top of the grouting element.

In the second example, the top element is defined as a coupled two-phase fully saturated element exposed to surface water pressure on the top surface (see Figure 33b). In the coupled problem, the deformation of the body and, consequently the total stresses and the transferred total normal stresses depend on both mechanical and hydraulic properties of the body.

For the verification of the implemented model, three cases are investigated: i) transfer of the load through a body with a very small mechanical stiffness (quasi fluid), ii) transfer of the load through a body with a stiffness equal to the contacted

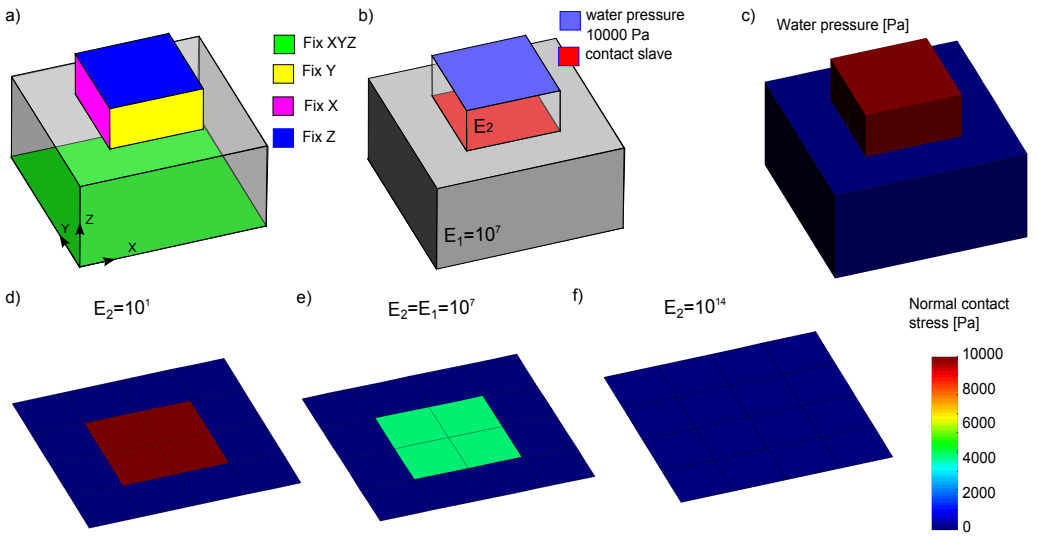

Figure 33: Verification of the contact model for a coupled-hydro mechanical problem—load transfer through a fully saturated porous material to the lining (slave contact) surface: a) DIRICHLET boundary conditions for the displacements ; b) loading (surface pressure of 10 kPa) and contact condition; c) constant water pressure in the body due to applied (no flow) boundary conditions; d) contact pressure due to load transfer through the body with very small stiffness (quasi fluid); e) contact pressure due to pressure transfer trough the body with moderately large stiffness E_2=10^7 N/m^2; f) contact pressure due to pressure transfer through the body with high stiffness E_2=10^{14} N/m^2.

body and iii) the transfer of the load through an almost undeformable (rigid) body. Since the boundary conditions applied in this study do not allow for water flow, in all three cases the resulting water pressure in the top element is constant and equal to the applied pressure (see Figure 33c).

In case (i), if a liquid pressure is applied on the body with almost zero stiffness, the resulting normal contact pressure on the bottom is equal to the applied pressure (total stress is equal to water pressure, see Figure 33d). Cases (ii) constitutes a coupled hydro-mechanical problem. In this cases, the normal contact pressure at the lining surface is reduced (Figure 33e). In the case of the rigid body (case (iii)), the transferred surface normal force is almost zero (Figure 33f). The mechanism of the development of the resulting stresses is explained in Figure 34.

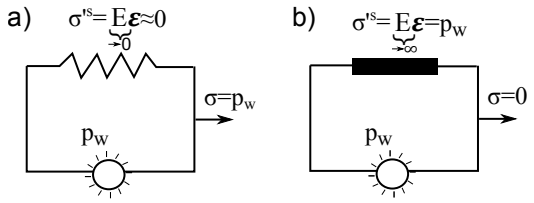

Figure 34: Schematic illustration of the hydro-mechanical stress transfer mechanism: a) Body with very low stiffness corresponding to the example shown in Figure 33d; b) Body with an infinitely high stiffness corresponding to the example shown in Figure 33f.

6.2. Assessment of quality of chosen spatial and temporal discretization

To assess the quality of the numerical solution in terms of the chosen element size and time discretization, we have performed consolidation analyses of a column containing five finite elements using the two-phase soil model introduced in Section 3, which represents a vertical column in the tunnel model emanating from the tail gap towards the surface (Fig. 35). The height of the column (h = 10m) corresponds to the overburden and the element size approximately corresponds to the discretization used in the tunnel model. A water water p_w=0 and a top surface load of t = 1 kPa are applied as boundary conditions at the top face and zero flux conditions are assumed at the bottom. The soil is assumed to be linear elastic with Youngs modulus of 50 MPa, Poissons ratio $\nu = 0.3$ and permeability $k_s = 10^{-6} ms$, corresponding to the upper soil layer. Also the same time discetization as used in the tunnel model was applied in this test. For this 1D consolidation

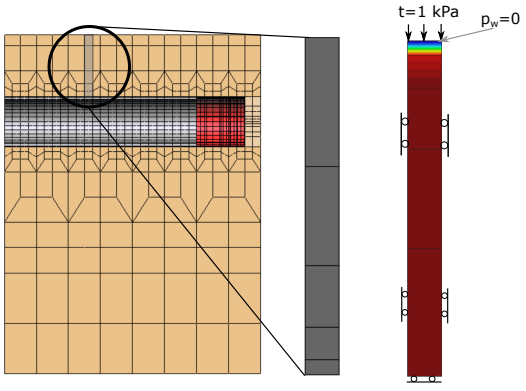

Figure 35: The discretization of the tunnel model and consolidation test model and boundary conditions of the consolidation test model.

problem the analytical solution according to Terzaghi (see e.g. (34)) is taken as the exact reference solution. The temporal evolution of the displacements and the spatial distribution of the pressure along the height according to the analytical solution for six different time instants are contained in Figure 36 . As can be observed from this figure, the spatial and temporal disretization used in this paper leads to an excellent agreement between numerical and analytical solution for the consolidation induced deformations, due to the quadratic approximation of displacements. Since a liner approximation of the liquid pressure is used, the quality of the reproduced water pressures for different time steps is less accurate, however still acceptable.

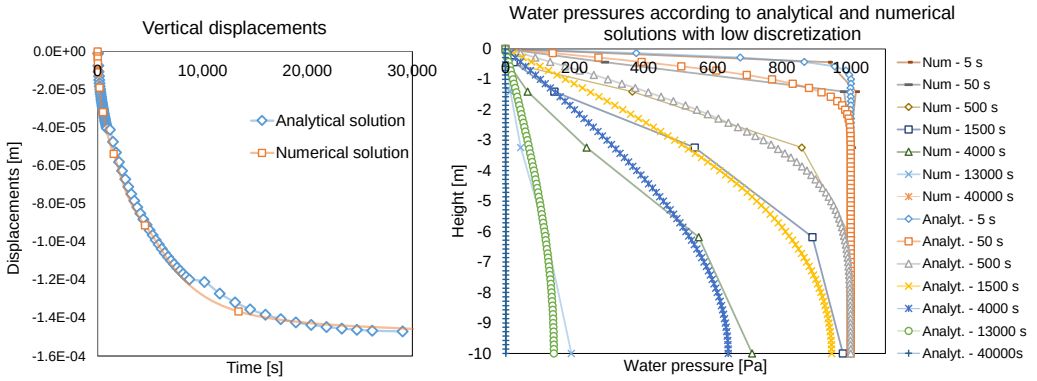

Figure 36: TERZAGHI's consolidation test: Development of surface settlements of the top surface in time and water pressure distribution in the soil column for different time steps.